

Nanoionic resistive-switching devices

*Xiaojian Zhu, Seung Hwan Lee and Wei D. Lu**

¹Department of Electrical Engineering and Computer Science, The University of Michigan, Ann Arbor, Michigan 48109, United States

*e-mail: wluce@umich.edu

KEYWORDS: Nanoionics, resistive switching effect, ionic processes, neuromorphic computing, reconfigurable nanostructures

Abstract:

Advances in the understanding of nanoscale ionic processes in solid-state thin films have led to the rapid development of devices based on coupled ionic–electronic effects. For example, ion-driven resistive-switching (RS) devices have been extensively studied for future memory applications due to their excellent performance in terms of switching speed, endurance, retention and scalability. Recent studies further suggest that RS devices are more than just resistors with tunable resistance; instead, they exhibit rich and complex internal ionic dynamics that equip them with native information-processing capabilities, particularly in the temporal domain. RS effects induced by the migration of different types of ions, often driven by an electric field, are discussed. It is shown that, by taking advantage of the different state variables controlled by the ionic processes, important synaptic functions can be faithfully implemented in solid-state devices and networks. Recent efforts on improving the controllability of ionic processes to optimize device performance are also discussed, along with new opportunities for material design and engineering enabled by the ability to control ionic processes at the atomic scale.

This is the author manuscript accepted for publication and has undergone full peer review but has not been through the copyediting, typesetting, pagination and proofreading process, which may lead to differences between this version and the [Version of Record](#). Please cite this article as [doi: 10.1002/aelm.201900184](https://doi.org/10.1002/aelm.201900184).

This article is protected by copyright. All rights reserved.

1. Introduction

For the past several decades, advances in electronics are driven by transistor scaling. Although ionic devices are also used in some systems, their roles are limited to bulky and slow components such as energy storage^[1], with a good example being Li-ion batteries. It has been long been acknowledged that an ionic device cannot compete with an electronic device in terms of speed, due to the much lower mobility of ions compared to that of electrons. However, in nanoscale devices this situation may no longer hold true. In a nanoscale film, a high electric field on the order of MV cm^{-1} can be readily achieved (e.g. by applying one volt to a film with a thickness of ten nanometers), and the speed of ionic processes can be exponentially increased at such high fields.^[2] The much lighter electron mass can now become a disadvantage, i.e. it can lead to tunneling through thin films to cause leakage current and data loss problems, while ions having a much higher effective mass can be more stable and be more reliably controlled. These controlled ionic processes in nanoscale solid-state devices have opened up promising opportunities for electronic circuit applications beyond energy storage. One representative example is ionic resistive switching (RS) devices (also called memristive devices or memristors)^[3-5], which can be used as a nonvolatile memory element due to its excellent performance such as high switching speed ($<1 \text{ ns}$)^[6], good retention ($>10 \text{ years}$)^[7], good endurance ($>10^9$)^[8] as well as high device scalability^[9].

The RS effect refers to the phenomenon that the resistance of a dielectric thin film, typically sandwiched between two electrodes, can be reversibly modulated by an electric field.^[2] In ionic RS devices, the mechanism originates from the rearrangement of atoms/ions in the dielectric thin film through ionic drift/diffusion and electrochemical processes that can lead to the formation/rupture of nanoscale conductive paths (filaments) between the two electrodes.^[10] Controlling these internal ionic processes will thus lead to better engineered devices with improved performance and reliability. Additionally, recent studies show that the internal ionic processes during RS can be used to faithfully emulate many biological processes and functions that are critical for learning and memory, allowing efficient neuromorphic systems to be implemented using solid-state devices and networks.^[11-13] Controlled ionic processes can also be used to directly modify the composition and/or structure of the material itself at the atomic scale, allowing new nanostructures to be built on the fly, in a reconfigurable fashion.

In this review, we will first discuss the switching mechanism of ion induced RS (memristive) effects in nanoscale solid-state thin films. Followed by discussions on controlling and utilization of the ionic effects to implement biological synaptic functions, and to reduce device variation and improve device stability. New concepts of material tuning enabled by controlled ionic process will be introduced at the end.

2. Ion induced Resistive switching (RS) effect

So far, ion-driven RS effects have been observed in a large variety of materials, ranging from oxides, halides to chalcogenides, etc.^[2, 13-15] Based on the types of ions involved during RS process, the switching mechanism can be divided to three categories: cation driven, anion driven and cation and anion jointly driven RS effects.

2.1 Cation driven RS effects

The origin of cation induced RS effect has been extensively studied and well understood in electrochemical metallization (ECM) devices, which are typically composed of an electrochemically active metal (e.g. Ag and Cu) electrode, an electrochemically inert metal (e.g. Pt) electrode, and an insulating switching layer (e.g. SiO_2) that acts as the host material for cation movement^[16-18] (Figure 1a). Using the Ag based ECM devices as an example, if a high enough positive bias voltage is applied on the active Ag electrode, the energy barrier for Ag ionization is sufficiently lowered and Ag atoms from the electrode will be oxidized into Ag^+ ions. The Ag^+ ions in turn permeate into the insulating dielectric layer and migrate toward the opposite inert electrode under the electric field. After receiving electrons injected from the inert electrode, Ag^+ ions are reduced to Ag atoms again and form Ag nanoclusters after a nucleation process. Continued growth of Ag nanoclusters eventually leads to the formation of Ag filaments that bridge the electrodes, and switch the device to the low resistance state (LRS) in this SET process (Figure 1b). Depending on the kinetic factors of the ions in the switching layer such as the ionic mobility and the redox (oxidation-reduction) rates, the growth dynamics and geometry of the filaments can be different.^[17] For example, the ionic mobility largely affects the growth direction of the filaments, where with a high mobility, the Ag^+ cations can readily reach the cathode and nucleate there, leading the filament growth from the cathode side; while low Ag^+ mobility can lead to ion reduction and nucleation inside the dielectric and growth of the filament from the anode side. On the other hand, the redox rate largely determines the denseness of the filament, where a high oxidation rate of the anode material can provide sufficient ions to form continuous and dense filaments whereas a low oxidation rate of the anode material results in the shortage of available ions and will form filaments composed of discrete nanoparticles (in the low mobility case) or with a branch shape (in the high mobility case).

Under a reversed bias voltage, the ion migration processes are reversed and can lead to filament rupture (Figure 1c), which switches the device to the high resistance state (HRS) in the RESET process. Since the formation of the filament directly changes the conduction mechanism from insulator (through the dielectric film) to metallic (through the filament), the ECM type devices usually show 'digital' RS behaviors, where an abrupt change of the device resistance with a high resistance ratio (typically $> 10^3$) is observed accompanying the RS process.^[19] Additionally, due to the high Gibbs free energy of formation of chemical compounds from Ag and the switching layer material, the Ag nanoclusters in the Ag filament generally has a good chemical stability (Figure 1d) and the filament is rather stable. Therefore, the ECM devices are promising candidates for memory applications.^[20]

Noble metals such as Pt and Pd have high oxidization potentials, thereby are usually used as the electrochemically inert electrodes and the electrochemical reaction of these metal atoms are neglected during RS process. However, recent investigation of Pt nanoparticles embedded in SiO_2 film indicates that even these inert nanoparticles can also go through redox processes, driven by a high enough electric field ($3\text{-}5 \text{ MV cm}^{-1}$).^[17] Indeed, the formation of filaments made of inert metals have recently been demonstrated in $\text{Pd/SiO}_x/\text{Pd}$ RS devices (Figure 1e).^[21] For the device at LRS, a filament formed inside the SiO_x film and bridged the Pd electrodes can be visualized (Figure 1f-g). Further composition analysis indicated that the filament was made of Pd, as shown in Figure 1h.

Moreover, the filament was found to grow from the anode toward the cathode and was composed of discrete Pd nanoparticles, suggesting that the mobility and the redox rate of Pd²⁺ ions in SiO_x dielectric film are low.

For a class of switching materials with very mobile cations, the movement of internal cations (vs. cations provided by an active electrode) can also lead to RS effects. These materials generally have cations forming weak ionic bonds with the immobile anions. The crystal structures in some materials may also provide native fast ion channels that facilitate the ion transport. A typical example is Li-containing materials such as Li_xCoO₂ that have been widely used as an electrode material for Li-ion battery applications.^[22] It was shown that Li_xCoO₂ has a layered structure composed of CoO₂ sheets with Li⁺ ions intercalated in between, and theoretical calculations suggest that the migration energy barrier of Li⁺ ions along the CoO₂ sheets is only 0.3 eV.^[23] In a RS device based on Li_xCoO₂ (Figure 1i-k), Li⁺ ions can be removed from the host material under an electric field and stored in a Li reservoir layer such as the doped-Si electrode, as illustrated in Figure 1k^[24]. The removal of Li⁺ ions can result in the generation of Li vacancies in the Li_xCoO₂ film and switch the device to the LRS.^[25] These Li vacancies can act as p-type dopants and increase the conductivity, and the modulation of the doping profiles can similarly explain the RS effects observed in Li_xFe₅O₈-based devices.^[26] Under a reversed bias voltage, the removed Li⁺ ions move back into the switching material, which increases the Li content and restores the device to the HRS.

Proton, i.e. H⁺ ion, is another example of highly mobile ions in solid-state films due to its light weight and small size. Upon the application of an electric field, protons, often acting as p-type dopants in films such as Bi₂Sr₂CaCu₂O_{8+δ}, can quickly redistribute in the switching material and modulate the device resistance^[27]. Specifically, in a moisture environment, water molecules in air can permeate into the dielectric film, and decompose into protons and hydroxide ions in the device to supply protons that potentially contribute to the RS effect.^[28]

Author

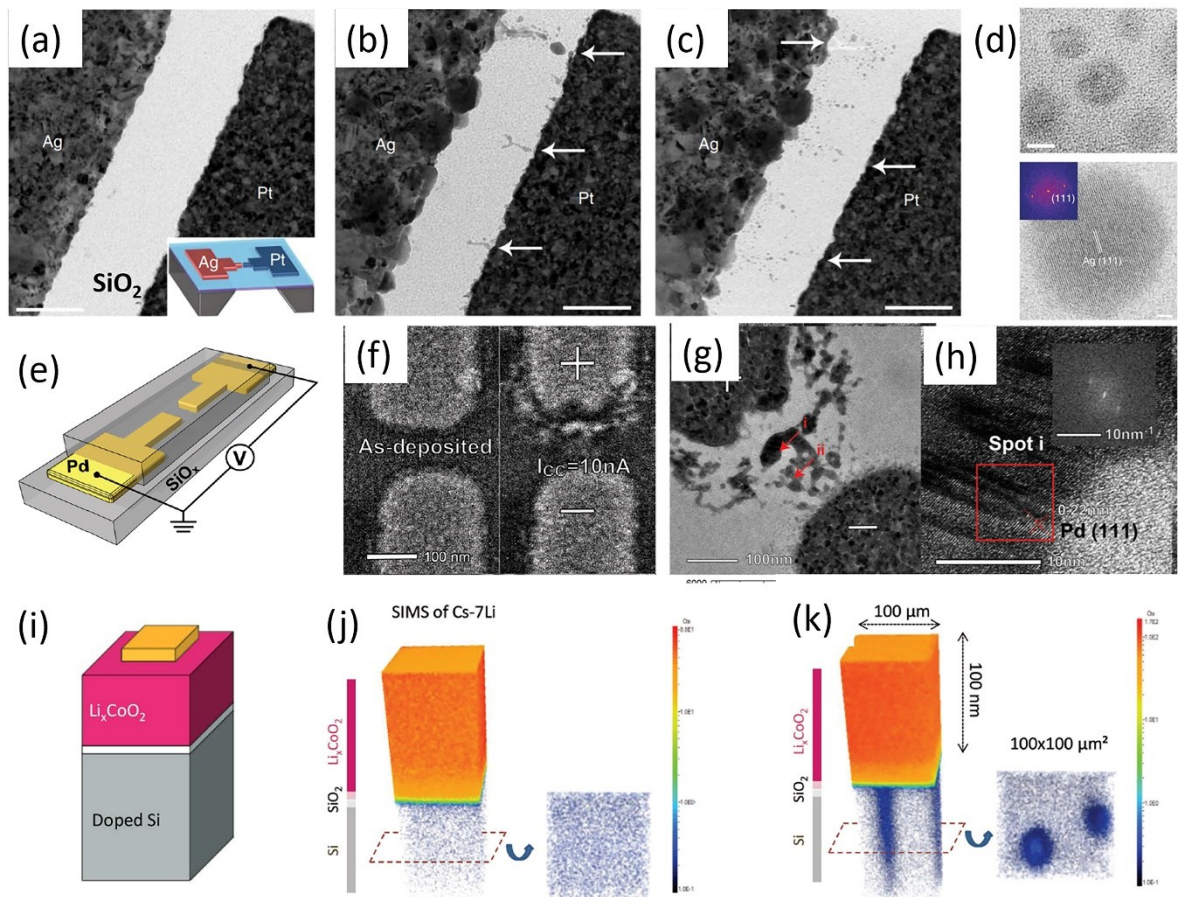


Figure 1. RS devices based on cations. a–c) TEM images of a Ag/SiO₂/Pt planar device in a) pristine state, b) LRS state, and c) HRS state. The arrows in (b) and (c) highlight the Ag filaments. Scale bar = 200 nm. d) Top: HRTEM image showing a group of nanoparticles inside the Ag filament in a Ag/a-Si/Pt device. Bottom: Bright-field STEM image of a Ag nanoparticle. The lattice fringes were indexed to the Ag fcc structure. Scale bar = 2 nm. Inset: fast Fourier transformation results of the HRTEM image. Reproduced with permission.^[16] Copyright 2012, Springer Nature. e) Schematic illustration of a Pd/SiO_x/Pd device. f) SEM images of an as-deposited Pd/SiO_x/Pd device and the device after SET. g) TEM image of the Pd/SiO_x/Pd device after SET, showing the filament formation. h) HRTEM of spot *i* (shown in (g)) where the inset FFT image indicates the crystalline nature of the Pd nanoparticles of the filament. Reproduced with permission.^[21] Copyright 2016, Royal Society of Chemistry. i) Schematic view of a Au/Li_xCoO₂/Si device. j,k) Cs-7Li signal mapping in the device in j) pristine state and k) LRS state. Left: 3D distribution of Cs-7Li signals. Right: Cumulative counts of Cs-7Li signals inside the silicon substrate, projected on a horizontal plane. In pristine state, low Li concentration was found in the doped Si substrate. At LRS state, two discoid zones (~20 μm in diameter) with a high Li concentration were found in the doped Si substrate, indicating the migration of Li⁺ ions into the Si substrate during RS. Reproduced with permission.^[24] Copyright 2018, John Wiley & Sons, Inc.

2.2 Anion driven RS effects

For most oxide-based RS devices, the oxygen ions (or equivalently, oxygen vacancies, V_{O_s}) are believed to be the mobile ions that drive the RS effect.^[29-31] In general, these devices are composed of two oxide layers sandwiched between a pair of electrochemically-inert electrodes, with one layer rich of V_{O_s} , and the other deficient of V_{O_s} and serving as the switching layer. The V_{O_s} -rich layer is usually made of non-stoichiometric suboxides (e.g. TaO_x) or metals (Ta) that can react with the switching layer to create a suboxide interface. In contrast, the switching layer is usually stoichiometric and insulating (e.g. Ta_2O_5), and has a high electrical resistivity when fabricated. Under a bias voltage, the neutral V_{O_s} in the V_{O_s} -rich layer lose electrons and become positively charged, and then migrate into the switching layer. These charged V_{O_s} can be reduced and eventually form V_{O_s} -rich regions that increase the device's conductance. Analysis of V_{O_s} -based conducting filaments have been carried out by TEM studies. For example, for TiO_2 based devices (**Figure 2a**), the conducting filaments may be composed of a metallic phase (Ti_4O_7) that has an increased Ti/O atom ratio (Figure 2b).^[32] In contrast, for Ta_2O_5 based devices (Figure 2c), the conducting filaments were found to be an oxygen deficient amorphous Ta (O) solid solution (Figure 2d-e).^[33] Notably, a high-temperature tetragonal α - Ta_2O_5 nanocrystal (as marked by the closed curve in Figure 2c) near the conducting filament was observed, indicating that Joule heating could be significant during RS, where the elevated temperature in this case caused the amorphous TaO_x film surrounding the filament to be annealed and converted into tetragonal α - Ta_2O_5 nanocrystals. Indeed, Joule heating has long been considered as an important factor during RS, where the ionic drift and diffusion processes can be significantly accelerated by the elevated temperature^[34-36]. Since Joule heating requires only an electronic current, it can precede and subsequently help activate the ionic processes. As a result, it is possible to observe "threshold" switching phenomena caused by electric effects and Joule heating, prior to ionic-filament formation. For example, a few studies^[37-40] have pointed out that in memristive devices based on such as TaO_x ^[40] and NbO_x ^[38] films, the applied bias can generate pronounced Joule heating through electron conduction (e.g. via the Poole-Frenkel process) that increases the device's internal temperature. The elevated temperature in turn speeds up the electron conduction, forming a positive feedback and leading to the formation of local hot conducting channels that lead to a sharp increase in device conductance.^[40] Note that when the device resistance is reduced, the Joule heating effect is also suppressed which will induce the negative differential resistance behavior and restores the device to the HRS, showing threshold RS effect.^[40] As such, this volatility can be used as an indication that distinguishes the electronic process induced switching effects from that caused by ionic process.

Another evidence of thermal effects can be seen from the ring-like structures of the V_{O_s} distribution observed through O K-edge X-ray absorption spectromicroscopy.^[36] The ring-like structures can be explained by the radial temperature gradient around the V_{O_s} filament. The temperature gradient produces a thermophoretic force that drives oxygen ions outward from the V_{O_s} filament region. This effect is countered by the inward diffusion of oxygen ions driven by the concentration gradient. At steady state, these two effects balance each other, producing an oxygen ion profile featuring a ring of oxygen interstitials around the filament and an inner core of oxygen vacancies.

For transition metals that have a high solubility of oxygen (e.g. Ta), the resistivity of the oxides depends on the V_O concentration, where a higher V_O concentration leads to a lower resistivity. Since no metastable phases exist for Ta_2O_5 at room temperature, the V_O concentration can be continuously tuned, leading to analog RS behaviors where the device resistance can be gradually adjusted.^[41] At high enough V_O concentrations (e.g. $5 \times 10^{20} \text{ cm}^{-3}$), the wavefunctions of the defects (V_O s) start to overlap and extend throughout the film thickness, leading to a metallic type behavior in the LRS.^[42-43]

Several recent studies have also started to explore controlled ion migrations in materials such as organic-inorganic halides (e.g. $CH_3NH_3PbI_3$)^[44], which have attracted broad interest as a promising optoelectronic material for solar cell^[45], photodetector^[46], light-emitting diodes^[47] and lasers^[48] applications. It was found that well controlled RS effects can be achieved in organic-inorganic halides as well, where the RS behavior is likely due to the motion of halogen anions. For example, in the $Ag/CH_3NH_3PbI_3/Ag$ RS system (Figure 2f), it was shown that the I:Pb atomic ratio in the $CH_3NH_3PbI_3$ film can be significantly decreased at LRS, then partially restored at HRS. These observations support the model that iodine ions in the $CH_3NH_3PbI_3$ film can be driven by an electric field and the formation/rupture of iodine vacancy filaments induces the RS effect (Figure 2g-h).^[49] Moreover, more iodine vacancies were observed near the cathode, indicating the growth of iodine vacancy filaments was initiated from the cathode and extended to the anode. It is worthy to note that Ag was used as the anode during RS. However, instead of being used as a soluble electrode that produces mobile ions in ECM devices, here the Ag electrode serves as an iodine ion reservoir that stores the iodine ions from the switching layer through the formation of AgI_x complexes.

RS effects in two dimensional chalcogenides such as MoS_2 has also drawn much attention recently.^[50-53] Given the strong in-plane chemical bonds, manipulating the ion distribution in 2D chalcogenides by an electric field is initially thought to be unlikely. However, recent studies have indicated that sulfur ions in MoS_2 can possibly be moved by an electric field and leads to RS effects. For example, in a memristive device based on mechanically exfoliated MoS_2 (Figure 2i), it was found that applying 5000 strong programming pulses (20 V/2 ms) can lead to the modulation of the S:Mo atomic ratio, with an increased (decreased) atomic ratio near the anode (cathode) (Figure 2j-k).^[53] Considering that sulfur ions have a higher mobility than molybdenum ions, sulfur ions are more likely to redistribute during device programming, and sulfur vacancies can act as n-type dopants and modulate the Schottky barrier height at the electrode/ MoS_2 interface that leads to the observed RS behaviors. Sulfur vacancy-induced doping effect has also been used by Sangwan et al to explain the RS effect in devices based on CVD-grown monolayer MoS_2 film.^[52] The authors proposed that the accumulation and dissipation of sulfur vacancies near the grain boundaries between the electrodes account for the RS effects, as supported by photoluminescence (PL) studies which showed a high PL intensity at the grain boundary in LRS, consistent with a high-concentration of sulfur vacancies.

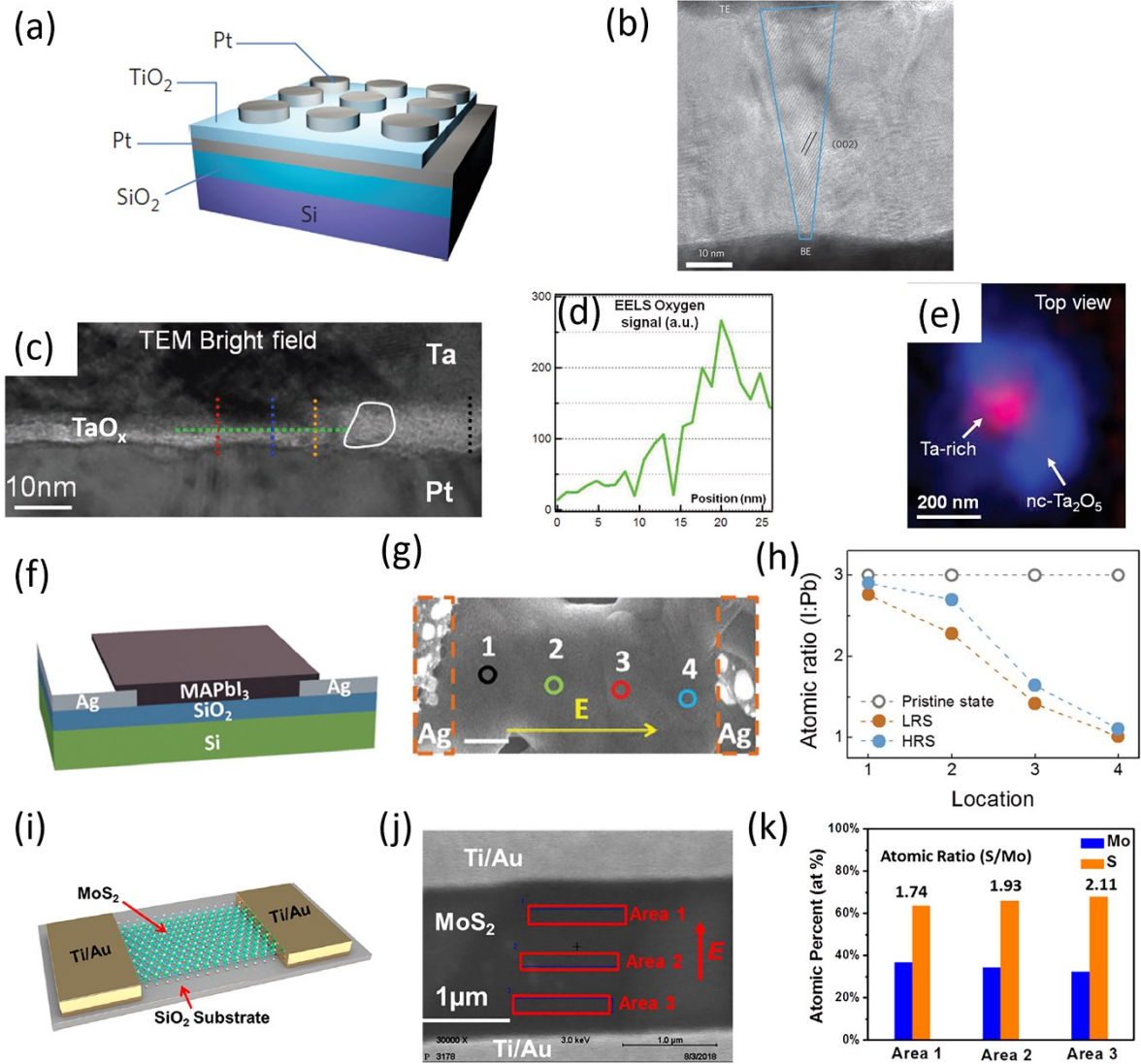


Figure 2. RS devices based on anions. a) Schematic of a Pt/TiO₂/Pt device. b) HRTEM image of a Ti₄O₇ region formed in the device in LRS state. Reproduced with permission.^[32] Copyright 2010, Springer Nature. c) Bright-field TEM image of a Ta/TaO_x/Pt device in LRS state. d) EELS oxygen profile along the green dashed line in (c), showing the decrease of the oxygen concentration in the filament region. e) Synchrotron-based nanobeam X-ray fluorescence measurement of a device, showing a central Ta-rich channel, surrounded by a nanocrystalline Ta₂O₅ phase. Reproduced with permission.^[33] Copyright 2015, John Wiley & Sons, Inc. f) Schematic of a planar Ag/CH₃NH₃PbI₃/Ag device. g) SEM image of a Ag/CH₃NH₃PbI₃/Ag device. Locations 1–4 mark the positions where the EDX analyses were performed. The dashed lines mark the locations of the Ag electrodes. Scale bar: 300 nm. h) Quantitative atomic ratio between I and Pb at locations 1–4 at the pristine, LRS, and HRS states, indicating the redistribution of iodine ions during RS process. Reproduced with permission.^[49] Copyright 2017, John Wiley & Sons, Inc. i) Schematic illustration of a few-layer MoS₂ device using Ti/Au electrodes. j) SEM images of a planar MoS₂ device after pulse stimulation. The red boxes mark the areas where the Mo:S atomic ratio was measured. k) Atomic ratio of Mo/S at areas 1, 2 and 3 as marked in (j), indicating the redistribution of sulfur ions during RS process. Reproduced with permission.^[53] Copyright 2018, American Chemical Society.

2.3 Cation and anion jointly driven RS effects

Rather than attributing the RS behavior to the motion of one specific type of ions, a few studies pointed out that the movement of cations and anions may coexist in some RS devices, involving different filament formation mechanisms. For example, for a typical VCM (Valence change memory) device, e.g. based on TaO_x , the RS effect is widely believed to be due to the motion of oxygen ions. However, a STM-based study suggests that Ta^{5+} cations can also migrate and possibly lead to RS behaviors in the TaO_x layer.^[54] Specifically, from the time dependent tunneling current measurements (Figure 3a), it can be seen that after the application of a negative bias voltage (-3 V) on the STM tip, a temporarily stable filament with a conductance higher than one quantum conductance can be formed in the vacuum gap between the STM tip and the TaO_x/Ta sample. This effect was attributed to the nucleation of Ta clusters on the surface of the TaO_x/Ta film that further led to the formation of a Ta metal filament. Similar effects were also observed in HfO_x/Hf and TiO_x/Ti structures. Visualization of filaments created by both cation and anion migrations has been demonstrated in the $\text{Ta}/\text{HfO}_2/\text{Pt}$ device (Figure 3b-e).^[55] At LRS, conduction channels that are both Ta-rich (Figure 3d) and O-deficient (Figure 3e) were observed in the HfO_2 switching layer, indicating both cations (Ta^{x+}) and anions (O^{2-}) may have moved. This result was attributed to the fact that Ta^{x+} cations and O^{2-} anions in HfO_2 have comparable mobility and migration energy barrier values. Under a SET voltage, the inward migration of Ta^{x+} cations from the Ta anode was accompanied by the simultaneous outward migration of O^{2-} where both Ta and V_O act as n-type dopants in the HfO_2 layer, and the accumulation of them switched the device to the LRS.

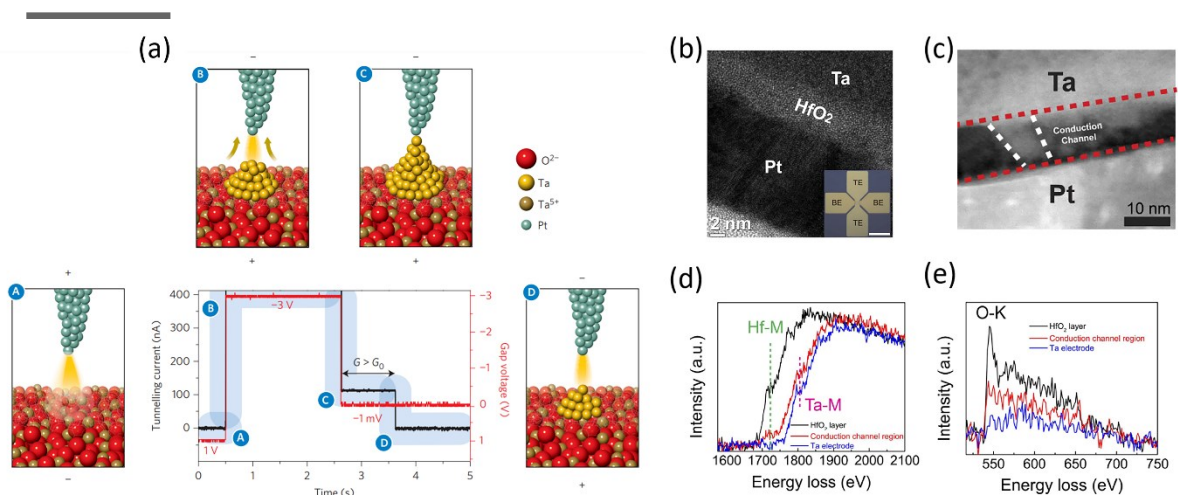


Figure 3. RS devices based on both cations and anions. a) Time dependence of the tunneling current measured on a 2-nm-thick TaO_x layer. The conductance G after a negative voltage pulse of -3 V was applied exceeded the conductance quantum G_0 , indicating the formation of a metallic quantum-point contact that is temporarily stable. Reproduced with permission.^[54] Copyright 2016, Springer Nature. b) TEM cross-section view of a $\text{Ta}/\text{HfO}_2/\text{Pt}$ device. c) HAADF-STEM image of a $\text{Ta}/\text{HfO}_2/\text{Pt}$ RS device in LRS state, showing a sub-10-nm conduction channel connecting Ta top and Pt bottom electrodes. d–e) Comparison of EELS spectra collected at the pristine HfO_2 layer, the conduction channel region, and the Ta electrode, indicating the conduction channel is both d) Ta rich and e) O deficient. Reproduced with permission.^[55] Copyright 2016, Springer Nature.

3. Ionic RS devices for neuromorphic computing

Beyond memory applications, the ability to tune ion distribution in solid-state devices allows efficient neuromorphic systems to be built with RS devices, where high density and large connectivity are necessary for the successful implementation of artificial neural networks. Specifically, in the brain, the information is encoded in spike firing patterns, which are transmitted among neurons through the synapses.^[56] The connection strength of the synapse, called synaptic weight, determines how efficient the input spikes can be propagated.^[57] Additionally, the synaptic weight can be updated by the neuron firing and the new weight can be maintained (an effect called synaptic plasticity^[58]). To this end, a memristive device showing analog RS behaviors is analogous to a synapse, where its conductance, act as the synaptic weight, determines how effectively an input pulse from one side (i.e. pre-synaptic side) of the device can produce output current at the other side (i.e. post-synaptic side) of the device. **Figure 4a** compares the role of a biological synapse with that of an ionic memristive device in artificial neural networks, with the switching layer emulating the synaptic cleft that bridges circuit elements acting as presynaptic and postsynaptic neurons.^[59] Figure 4b represents one of the first demonstrations of this concept, and shows that the conductance of a Ag:Si/Si memristive device can be incrementally increased and decreased by applying positive and negative pulses, emulating the potentiation (weight increase) and depression (weight decrease) behaviors of a biological synapse, respectively.

Moreover, the internal dynamic ion processes in RS devices allow them to faithfully emulate the underlying physical and chemical processes in biological synapses, instead of simply implementing hand-crafted "rules". Specifically, most synapses in the brain are chemical synapses and their functions are mediated by the flow of ions.^[60-63] For instance, the influx of extracellular Ca^{2+} ions through ion channels in the pre- and post- synaptic neuron membranes can lead to a cascade of reactions that affect the synaptic weight, e.g. by regulating the amount of neurotransmitter releases from the presynaptic neuron or by modulating the number of AMPA receptors in the postsynaptic neuron. Recent studies have suggested these ionic processes can be emulated in ionic RS devices with similar dynamics, where pulses trains encoded with different temporal patterns can lead to diverse yet predictable conductance (weight) changes.^[64]

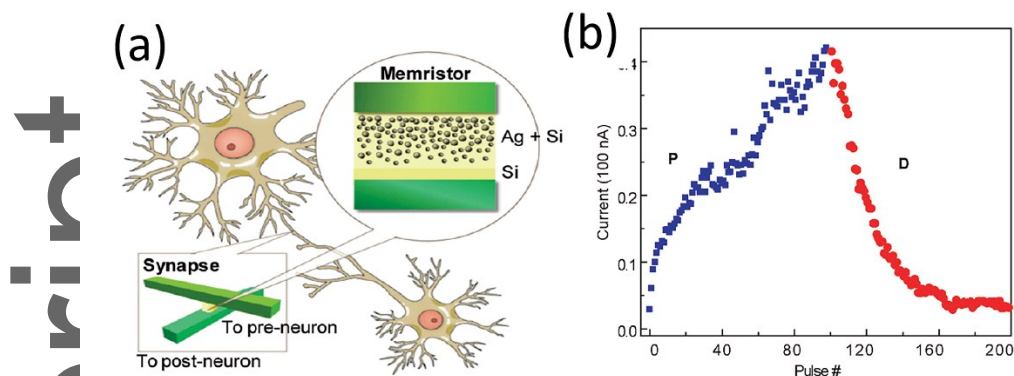


Figure 4. Using memristive devices as synaptic devices in artificial neural networks. a) Schematic illustration of the concept. The insets show the two-terminal device geometry and the layered structure of the memristor. b) Incremental conductance modulation of a memristor, in response to identical, consecutive potentiating (blue square) and depressing (red circle) pulses, emulating the plasticity behavior of a biological synapse. Reproduced with permission.^[59] Copyright 2010, American Chemical Society.

In general, synaptic plasticity can be divided to two groups: homosynaptic plasticity and heterosynaptic plasticity, where homosynaptic plasticity refers to synaptic weight changes that are only affected by the stimulation applied to the synapse in question itself, and heterosynaptic plasticity refers to the effect that the weight change in a synapse is also dependent on stimulations applied to other synapses.

3.1 Homosynaptic plasticity

Homosynaptic plasticity is typically input-specific, and the changes take place only at the stimulated synapse, not at other unstimulated synapses. Short-term and long-term memory effects are two main examples of homosynaptic plasticity.

The short-term memory (STM) effect (e.g. short-term potentiation/depression, STP/STD) refers to effects where the synaptic weight changes are temporary.^[65] The memory effect of STM typically lasts for tens of milliseconds to minutes. The mechanism of STP can be possibly explained by the Ca^{2+} dynamics in the presynaptic neuron, where an increase of the intracellular Ca^{2+} concentration (induced by the spike stimulation) enhances the neurotransmitter release probability and thus increases the synaptic weight. Whereas after removing the spike stimulation, the spontaneous decay of Ca^{2+} concentration (induced by Ca^{2+} extrusion process) restores the neurotransmitter release probability and also the synaptic weight to the original state.^[61]

The spontaneous decay of Ca^{2+} concentration can be emulated by spontaneous ion diffusion out of the conduction channel in RS devices, which naturally leads to a volatile (i.e. short-term) memory effect. For example, under weak stimulation conditions, the filament is formed by a small number of ionic defects (e.g. V_{OS}).^[66] These filaments are unstable and spontaneous diffusion of the V_{OS} can readily weaken the filaments and even disrupt them, as illustrated in **Figure 5a**, which brings the device back to the HRS state. Figure 5b shows a retention curve of a $\text{W}/\text{WO}_x/\text{Pd}$ memristor, exhibiting characteristic STM effect. The memory loss usually shows a rapid initial decay phase

followed by a slower decay over a long time period, and can be described by a stretched-exponential function that is commonly used to depict the electronic or structural relaxation effects observed in disordered material systems.^[66]

In contrast to the STM effect which is temporary and transient, the long-term memory (LTM) effect is stable and persistent. LTM effects (e.g. long-term potentiation/depression, LTP/LTD) mainly refer to synaptic weight changes that last from minutes to months, or even to a lifetime, and are related to more pronounced changes in the synapse.^[67] For example, LTP may be facilitated by the increase of intracellular Ca^{2+} ion concentration in the postsynaptic neuron that leads to the synthesis of plasticity related proteins (PRPs), which can in turn promote synapse growth either through the formation of new dendrites or enhancing the activities of existing ones.^[68]

LTM effects can be emulated in RS devices with strong filament that can tolerate ion/atom diffusion (Figure 5c). Additionally, in biology as well in RS devices, STM can be transitioned to LTM after a consolidation process through repeated stimulation. This effect has been demonstrated in memristive devices by increasing the number of stimulation pulses, which leads to cumulative ionic defect (e.g. V_{O}) accumulation and filament growth that results in more stable filaments. As shown in Figure 5d, a $\text{W}/\text{WO}_x/\text{Pd}$ device when programmed with five stimulation pulses shows fast memory loss, whereas by increasing the number of stimulation pulses to 40, a much slower conductance decay process and better memory retention were observed, due to the formation of stronger filaments.^[66, 69-70]

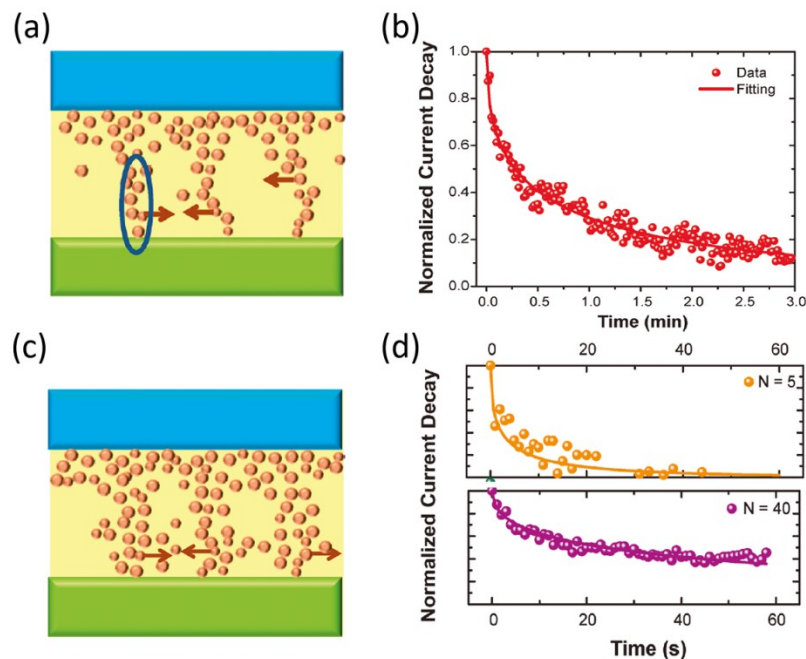


Figure 5. STM and STM-LTM transition in a $\text{W}/\text{WO}_x/\text{Pd}$ memristive device. a) Schematic illustration of V_{O} diffusion in the device, which leads to rupture of weak V_{O} filaments. b) A retention curve after SET, showing the STM effect. The experimental data was fitted by a stretched-exponential function. c) Schematic showing the formation of strong V_{O} filaments that are tolerant of V_{O} diffusion. d) Memory retention data recorded after the stimulation of (top panel) 5 pulses and (bottom panel) 40

pulses, showing improvement of memory retention with increased stimulation pulse number. Reproduced with permission.^[66] Copyright 2011, American Chemical Society.

By taking advantage of the underlying dynamic ionic processes during RS, it has been shown that memristors are capable of naturally emulating short-term and long-term homosynaptic behaviors, including paired pulse facilitation (PPF), spiking rate dependent plasticity (SRDP) and spiking timing dependent plasticity (STDP), without resorting to specially engineered programming pulses and circuits.^[71-77] Specifically, in biological systems the different synaptic plasticity behaviors are closely related to the dynamics of intracellular Ca^{2+} concentration, which increases after a pre-synaptic spike and spontaneously decays afterwards. The short-term dynamics of Ca^{2+} concentration effectively provide a local timing mechanism that allows the synapse to naturally respond to the temporal spiking events, and lead to behaviors such as PPF, STDP and SRDP without needing a global clock in the system.

Mathematically, the memristive effect can be described in the theoretical framework proposed by Chua et al, using the following equations^[78]:

$$I=G(w, V, t)V \quad (1)$$

$$\frac{dw}{dt} = f(w, V, t) \quad (2)$$

Here, equation (1) corresponds to the I-V relationship of the device and w represents the state variable that determines the device conductance (such as the filament size^[79]). Equation (2) is the dynamic equation of w and enables synaptic plasticity. In the simplest case, the evolution of the state variable w is only dependent on the external inputs, such as the pulse amplitude and duration. Recent studies^[71-72, 80-81], however, show that w is also dependent on other, “second-order” state variables such as the ion mobility^[72] and local temperature^[71]. The dynamic equation of the “first-order” state variable w can then be updated and expressed as

$$\frac{dw}{dt} = f(w, T, V, t) \quad (3)$$

where T represents the second-order variables. More importantly, these second order state variables^[71-72] may have short-term dynamics and can essentially play a similar role of Ca^{2+} concentration in biological systems. For example, a spike (e.g. a voltage pulse) can cause the device’s internal temperature to increase temporally, followed by a quick decay. Since the ion drift and diffusion strongly depend on the local temperature, the short-term dynamics of the internal temperature can be used to natively implement PPF, STDP and SRDP effects, following similar roles played by the short-term dynamics of Ca^{2+} concentration.

Similar effects can also be obtained with other second-order state parameters. For example, it is proposed that under a stimulation pulse, the V_0 s in the WO_x film can be driven out of equilibrium and gain an enhanced mobility^[72]. The increased V_0 mobility can facilitate V_0 migration, leading to a fast growth (or rupture) of the filament. The enhanced mobility is however temporary, and the short-term dynamics allow the system to natively respond to temporal stimulations. For example,

Figure 6a shows the implementation of the PPF effect by studying the device response with two identical pulses having different time intervals. A higher stimulation current is observed in the second pulse, and the increase is more pronounced when the second pulse is closer to the first pulse (Figure 6a). Such a trend can be more clearly observed by plotting the calculated change ratio (PPF ratio, measured as the current in the second spike over that in the first spike) against the time interval between the two spikes (Figure 6b). This behavior can be interpreted based on the increased V_0 mobility due to the first pulse, which in turn leads to a larger response in the second pulse. Since the mobility increase is only short-term, the extend of the mobility increase depends on the relative timing of the second pulse with respect to the first one, such that at longer intervals this effect becomes weaker resulting in a smaller PPF ratio. Based on the same effect, SRDP behaviors, where a higher frequency (smaller time interval) stimulation leads to a larger weight change, can be implemented as well (Figure 6c).

Spiking timing dependent plasticity (STDP) is another important synaptic learning rule, which refers to the effect that the sign and the magnitude of the synaptic plasticity depend on the relative timing of the pre-synaptic spike and the post-synaptic spike.^[82] For example, if the presynaptic spike arrives earlier than the postsynaptic spike, the events will lead to an overall synaptic weight increase; whereas reversing the time sequence will lead to weight decrease. Additionally, the shorter the time interval is, the higher degree the weight change is. This effect can also be implemented with the WO_x based memristors, by using the internal short-term dynamics to naturally decode the relative timing information of the pre- and post-synaptic spikes, as shown in Figure 6d.

Author Manuscript

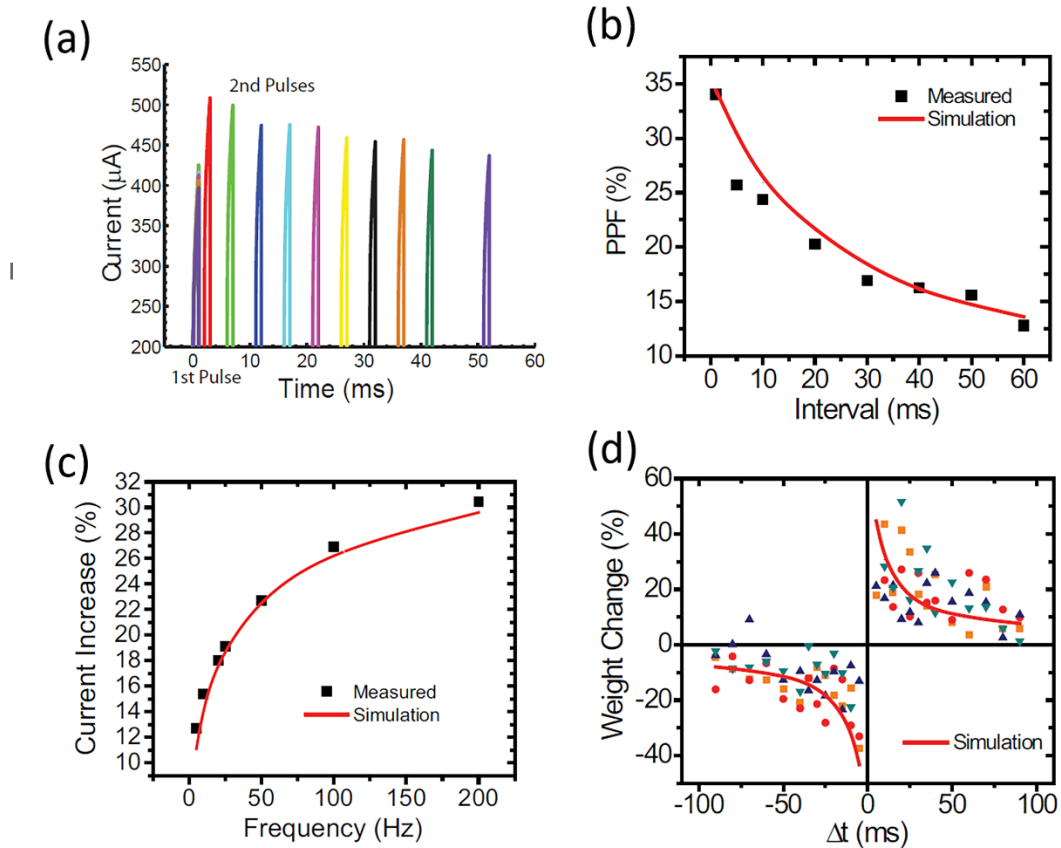


Figure 6. Biorealistic implementation of PPF, SRDP, and STDP effects in WO_x -based memristive devices by utilizing the dynamics of ionic mobility. a) Current response to the application of paired pulses (1.4 V, 1 ms) in a device, at ten different pulse intervals. The second pulse in the pulse pair produces an enhanced response in all cases and increasing the pulse interval leads to a decrease in the enhancement. b) PPF ratio as a function of pulse interval. c) Change in memristor current after the application of pulse trains with different frequencies. Higher stimulation frequency leads to a larger conductance enhancement. d) Memristor weight change as a function of the relative timing between the pre- and post-synaptic pulses, showing STDP behavior. Reproduced with permission.^[72] Copyright 2015, John Wiley & Sons, Inc.

As briefly mentioned earlier, the local temperature T is another second-order state variable that can play a similar role to that of Ca^{2+} concentration. Specifically, a programming pulse can elevate the local temperature T due to Joule heating. The temperature rise can significantly enhance the drift and diffusion of ions, leading to a fast growth of the filament. The temperature would spontaneously decay after the removal of the programming pulse, showing a short-term effect. With a short interval, the elevated temperature has not fully decayed when the second programming pulse arrives. As a result, the device is subjected to a higher temperature during the second programming pulse, resulting in enhanced potentiation or depression effects driven by the pulse. The extent of the enhancement thus depends on the interval between the two pulses, as a shorter pulse interval leads to higher temperature seen by the second pulse and a larger conductance change, and vice versa. Utilizing this effect, SRDP and STDP effects have been implemented using

simple, non-overlapping pulses in TaO_x based memristive devices^[71] (Figure 7a-b). Note that to enhance the temperature effects in the study, weak heating pulses (with a low pulse amplitude) were used in addition to the stimulation pulses (with a high pulse amplitude), as shown in Figure 7a.

These effects have also been demonstrated in so-called “diffusive memristors”, which exhibit short-term memory effects due to ion/atom diffusion in weakly-formed filaments.^[73] For example, after a weak Ag filament was formed in the switching layer that increased the device conductance, the conductance would decay soon after the programming pulse is removed, due to the spontaneously nucleation of the continuous Ag filament into discrete Ag nanoparticles to minimize the surface energy. When this volatile device is connected with another nonvolatile memristive device in series, the short-term dynamics in the diffusive memristive device can serve as a second-order state variable to modify the long-term conductance changes of the nonvolatile memristor. Based on this concept, important synaptic behaviors such as SRDP and STDP effect have been successfully implemented, as shown in Figure 7c and 7d.

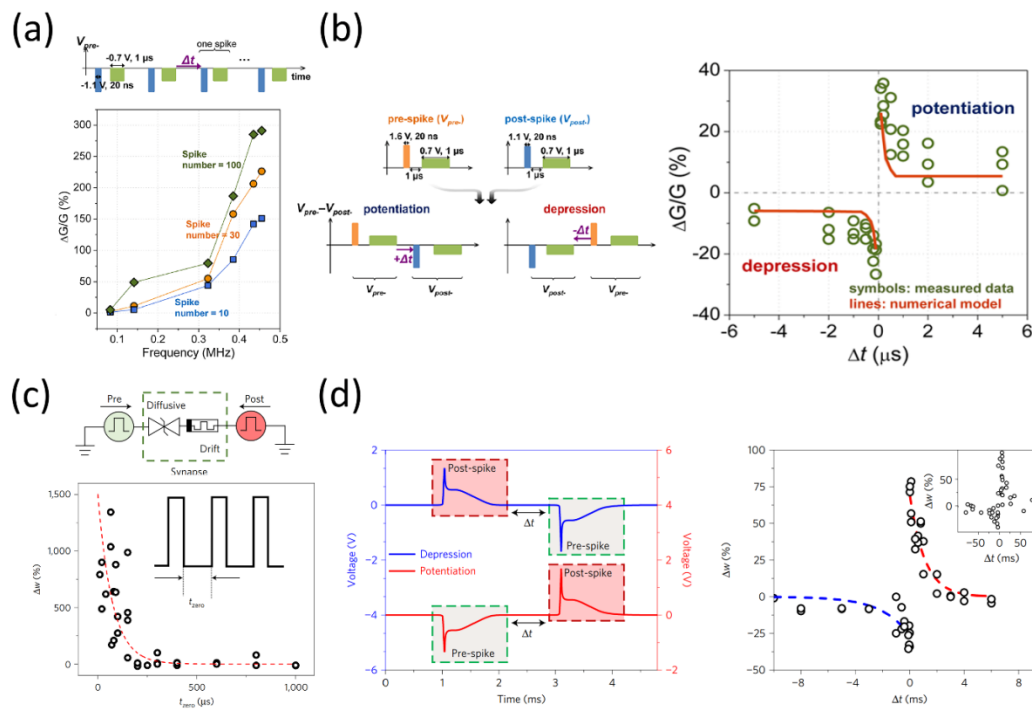


Figure 7. Natural implementation of SRDP and STDP effects in a second-order Ta₂O_{5-x}/TaO_y memristor and in a diffusive Ag: SiO_xN_y memristor connected in series with a TaO_x non-volatile memristor, respectively. a) Left: Spike pattern for the SRDP effect in a Pd/Ta₂O_{5-x}/TaO_y/Pd second-order memristive device. Each spike consists of a programming pulse and a heating pulse. Right: memristor conductance change as a function of spike frequency, for different number of spikes. b) Left: presynaptic and postsynaptic spikes used for the implementation of STDP effect. Right: conductance change ratio as a function of the relative timing between the pre- and post-synaptic pulses. Reproduced with permission.^[71] Copyright 2015, American Chemical Society. c) Upper: Circuit diagram showing a Ag: SiO_xN_y diffusive memristor connected in series with a TaO_x non-volatile memristor. Bottom: Conductance change of the TaO_x non-volatile memristor as a function of the

duration between the applied pulses, showing SRDP effect. d) Left: schematic of the pulses applied to the combined device for STDP demonstration. Right: plot of the conductance (weight) change of the nonvolatile memristor as a function of the relative timing between the pre- and post-synaptic spikes, showing STDP behavior. Reproduced with permission.^[73] Copyright 2017, Springer Nature.

Recent research has further shown that the ion dynamics allow the implementation of more complex homosynaptic functions, such as synaptic metaplasticity^[74-77]. Synaptic metaplasticity refers to the effect that the prior history of activities affect current synaptic plasticity, including both the direction (potentiation or depression) and the degree of weight changes.^[83] Since different activity histories may result in the same synaptic weight, emulating metaplasticity with commonly used first-order memristors is not feasible since the synaptic plasticity in these devices is only determined by the current synaptic weight (determined by the state variable w , e.g. filament size) and current inputs, e.g. equation (2). Instead, synaptic metaplasticity needs to be realized in memristors with a set of internal state variables.^[74]

For example, the effective filament size can be decomposed to a set of state variables representing the filament position, width and length. Even at the same conductance conditions, these internal parameters may be different and can evolve following their own dynamics in the form of equation (3), and lead to different device conductance changes (synaptic plasticity). This type of history dependent plasticity is implemented by using the filament position as the state variable in a Pt/Ta₂O_{5-x}/TaO_y/Pt memristive device, which shows complementary resistive switching (CRS) effects.^[74] The CRS effect is characterized by an initial conductance increase followed by a decrease during the SET process, and is attributed to the depletion of V_o at the V_o source region when the device is overprogrammed. Therefore, the device showing a high resistance value can have two different filament configurations, with the filament rupture position near the top or the bottom electrode, as shown in **Figure 8a** and **8b**, respectively. In this case, under the same positive pulse stimulation conditions, the filament can either shrink if the filament was ruptured at the top electrode (e.g. the situation shown in **Figure 8a**), or grow if the filament was ruptured at the bottom electrode (e.g. the situation shown in **Figure 8b**), leading to opposite conductance changes.

Figure 8c shows the measured conductance of the Pt/Ta₂O_{5-x}/TaO_y/Pt device as a function of the pre-programming conditions. After using different numbers of pre-programming pulses to switch the device to state A and state B that exhibit apparently identical conductance values, continued stimulation of the device with identical stimuli leads to opposite synaptic plasticity polarities, as shown in **Figure 8d**. Similarly, after using different frequencies of pre-programming pulses to switch the device to the same conductance values (but with opposite filament rupture positions, **Figure 8e**), opposite synaptic polarity can be also obtained (**Figure 8f**).

The activity dependence of the synaptic plasticity degree can similarly be implemented, by employing the filament width and length as the state variables. It is known that filament growth involves ion drift driven by the electric field as well as ion diffusion driven by the concentration gradient.^[84-85] Since ion drift depends exponentially on the applied field, at a high SET voltage ion drift dominates and can lead to a narrow and long filament (represented by the high V_o concentration region in **Figure 8g**), while at low field drift becomes less pronounced and a wide and

short filament can be formed instead due to a larger diffusion component (Figure 8h). Afterwards, these two configurations may show similar conductance, but the narrow and long filament case can show a higher degree of synaptic plasticity due to the enhanced field between the filament tip and the electrode, compared to the wide and short filament case. This effect is indeed verified experimentally, as shown in Figure 8i, where a more pronounced conductance change can be observed if the device was initialized by a high pre-programming voltage that presumably led to a longer and narrower filament. Similarly, during RESET a high voltage can lead to pronounced Joule heating and facilitate V_O dissipation, leading to the formation of a highly insulating gap with minimal number of residual V_O s, as shown in Figure 8j. On the other hand, a low RESET voltage will create a less insulating gap with a higher concentration of residual V_O s, as shown in Figure 8k. At the same HRS, the device having a more insulating gap corresponds to a smaller gap size, thus can produce a higher degree of plasticity under further stimuli (Figure 8l).

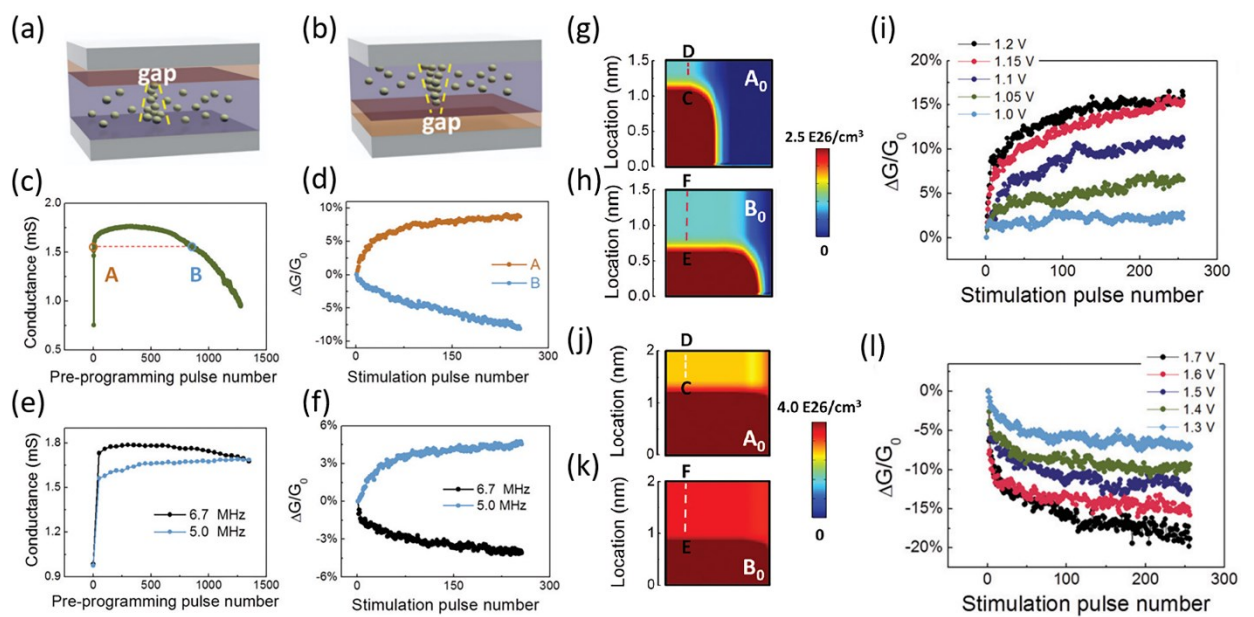


Figure 8. Implementation of synaptic metaplasticity. a–b) Schematics of V_O distributions in a Pt/Ta₂O_{5-x}/TaO_y/Pt device at HRS, with the V_O filament rupture positions near a) the top electrode and b) the bottom electrode. c) Dependence of the device conductance on the number of applied pre-programming pulses (1.2 V, 0.5 μ s). d) Conductance changes in the device at state A and B (marked in (c)) as a function of the number of applied stimulation pulses (1.1 V, 0.5 μ s), showing potentiation and depression behaviors respectively. e) Evolution of the device conductance with pre-programming pulse frequencies of 6.7 MHz and 5.0 MHz, respectively. f) Conductance changes of the device in (e), as a function of stimulation pulse number, showing activity-dependent potentiation and depression behaviors, respectively. g–h) Simulated 2D maps of V_O concentration distributions in a device with g) a narrow and long filament and h) a wide and short filament. i) Conductance changes in a device after being pre-programmed using SET pulses with different amplitudes, showing different degrees of synaptic plasticity. j–k) Simulated 2D maps of V_O concentration distributions in a device with j) a low V_O residue concentration in the gap and k) a high V_O residue concentration in the gap. l) Conductance changes in the device after being pre-

programmed using RESET pulses with different amplitudes, showing different degrees of synaptic plasticity. Reproduced with permission.^[74] Copyright 2017, Royal Society of Chemistry.

3.2 Heterosynaptic plasticity

Heterosynaptic plasticity refers to the effect that synaptic changes are not just input specific, but can also be induced by the activity of other neurons.^[86] For example, a stimulated synapse can affect another, unstimulated synapse. Heterosynaptic plasticity is believed to be critical for neural processes such as associative learning, and for the stability of the neural network.

In biology, synaptic interaction effects include synaptic competition and synaptic cooperation. These effects are in turn driven by the internal molecular/ion processes, e.g. the exchange of diffusive plasticity related proteins (PRPs) among multiple synapses through the dendrite of the postsynaptic neuron.^[87] Specifically, synaptic competition can be attributed to the competition among synapses for a limited amount of PRPs for their growth, while synaptic cooperation originates from the sharing of PRPs among adjacent synapses that leads to synergistic synaptic growth. To closely emulate the synaptic interactions observed in biological systems, utilizing internal ionic processes that play a role similar to the PRP dynamics to allow direct coupling among synaptic devices is thus necessary.

Recently, synaptic interaction behaviors were successfully demonstrated in the Li_xMoS_2 system by employing direct ionic coupling effects.^[88] The emulated neural network has a planar structure, composed of multiple adjacent $\text{Au}/\text{Li}_x\text{MoS}_2/\text{Au}$ devices as shown in **Figure 9a**. These devices share a common Au/MoS_2 region that resembles the synaptic terminals on the dendrite of the postsynaptic neuron, while the other Au electrodes represent the presynaptic terminals (Figure 9b). Similar to PRP diffusion, the diffusion of Li^+ ions allows ionic coupling among multiple devices, which is enabled by the layered van der Waals structure in the MoS_2 film that allows the Li^+ ions to move relatively freely in between the MoS_2 layers. As a result of Li^+ ion migration into (out of) the postsynaptic terminal region, conductance increase (decrease) of the MoS_2 film can be observed, accompanied with possible structural changes and semiconductor-metal phase transitions.^[88]

Synaptic competition effect was first demonstrated in such a system consisting of two adjacent synaptic devices with a limited amount of Li^+ ions. These limited Li^+ ions were initially stored at the postsynaptic terminal region and were used to emulate the situation of scarce PRPs (Figure 9c). Note the Li^+ ion intercalation in MoS_2 can lead to the increase of interlayer distance, which allows these processes to be visualized by measuring the film's height changes, e.g. through AFM studies. Afterwards, the Li^+ ions were allocated to the two devices under controlled bias voltages, resulting in configuration I (Figure 9d) and configuration II (Figure 9e), corresponding to cases where device 1 (2) has more Li^+ ions, respectively. The synaptic potentiation/depression behaviors of the two devices at configuration I and II are shown in Figure 9f and 9g. It was observed that the device having more Li^+ ions exhibits a higher degree of synaptic potentiation/depression, and increasing the amount of Li^+ ions allocated to one device (e.g. device 2) would enhance its synaptic plasticity, while suppressing the synaptic plasticity in the other device (e.g. device 1), due to competition between the two devices for the limited Li^+ ion supply.

Synaptic cooperation effects were also demonstrated in the Li_xMoS_2 system by emulating the sharing of PRPs. In a system consisting two adjacent synaptic devices as shown in Figure 9h, Li^+ ions were initially accumulated in device 1 under electrode A (configuration I). As a result, the potentiation effect in device 2 initially cannot be induced (black curve in Figure 9j). After the potentiation of device 1 (Figure 9k), Li^+ ions under electrode A were driven toward electrode B and led to configuration II, as illustrated in Figure 9i. The Li^+ ions under electrode B now allow device 2 to exhibit synaptic potentiation behavior when the same stimulation pulses are applied (red curve in Figure 9j). These results suggest that potentiation of one synaptic device can facilitate the plasticity of a neighboring synaptic device. Moreover, in a network-type system composed of four adjacent synaptic devices, programming one of the synaptic devices (Figure 9l) was shown to not only affect the weight of the stimulated synaptic device, but also synergistically modulated the weights of the other, unstimulated synaptic devices, as demonstrated in Figure 9m. Ionic coupling effects in these memristive systems can allow more faithful implementation of complex synaptic functions for neuromorphic computing applications, without having to resort to external circuitry or software implementations.

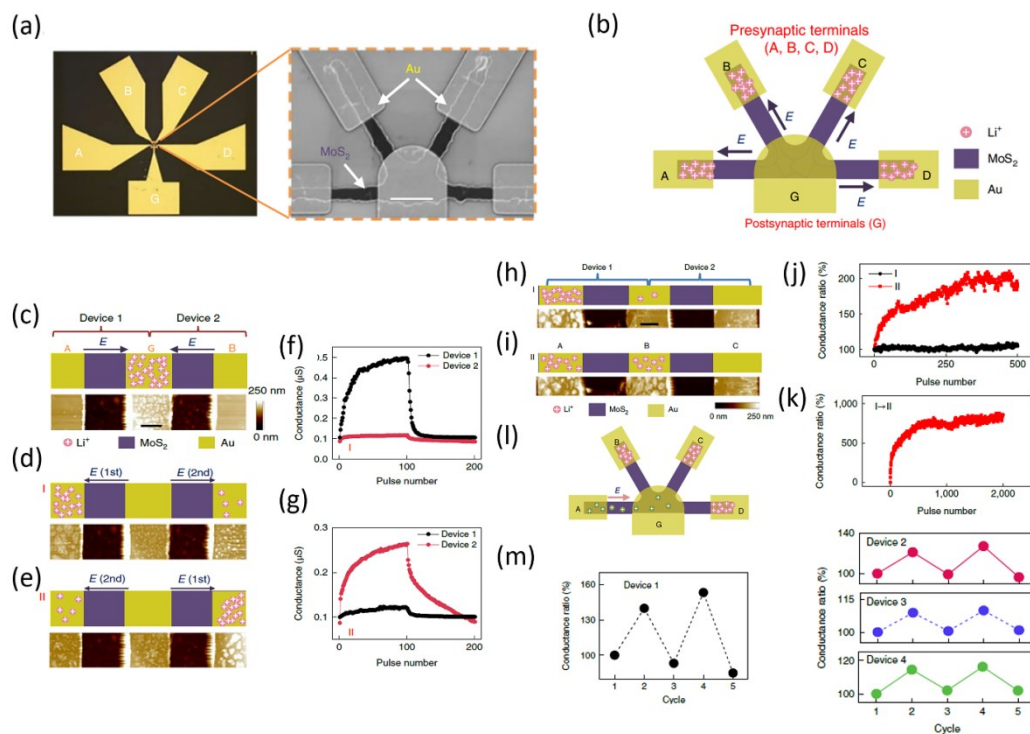


Figure 9. Implementation of synaptic interaction effects in Li_xMoS_2 memristive devices. a) Optical (left) and scanning electron (right) micrographs of four devices forming a network structure. Scale bar = $5 \mu\text{m}$. b) Schematic of the Li^+ ion distribution in the network under the initial conditions, with depletion of Li^+ ions under electrode G. c–e) Schematics showing the distribution of Li^+ ions (top panel), and AFM height images (bottom panel) of devices 1 and 2, for c) when all Li^+ ions are accumulated under electrode G; d) configuration I, where most Li^+ ions are accumulated under electrode A; and e) configuration II, where most Li^+ ions are accumulated under electrode B. f–g) Synaptic potentiation/depression effects of the two devices in configuration I and configuration II.

h–i) Schematics of the Li^+ ion distribution (top panel), and AFM height images (bottom panel) of a system consisting of two devices. Scale bar = 2 μm . Starting from configuration I (h), where most of the Li^+ ions in the system accumulate under electrode A, after potentiation of device 1, some Li^+ ions migrate towards electrode B, creating configuration II (i). j) Potentiation behaviors of device 2, showing no response at configuration I and effective potentiation at configuration II. k) Evolution of the conductance of device 1 when the system was changed from configuration I to configuration II. l) Synaptic cooperation in a network of four devices, illustrating the process that a positive bias on electrode A drives Li^+ ions towards electrode G and potentiates device 1. m) Potentiation and depression cycles of device 1, and the corresponding conductance changes in non-stimulated devices 2, 3 and 4. Reproduced with permission.^[88] Copyright 2019, Springer Nature.

Modulatory input-dependent plasticity is another form of widely studied heterosynaptic plasticity in biology, describing effect that the firing of a modulatory neuron can regulate the connection strength between a presynaptic neuron and a post-synaptic neuron.^[89] This effect was demonstrated in a multi-terminal planar memristive system composed of self-organized Ag nanoparticles (Figure 10a-b).^[90] Electrical pulses applied on a pair of Pt electrodes that represent the presynaptic and the postsynaptic terminals drive the electrochemical reaction and the redistribution of the discrete Ag nanoparticles, and lead to the formation of continuous Ag filaments between the electrodes (Figure 10c), corresponding to synaptic potentiation (SET process). By applying a constant bias voltage on another electrode, acting as the modulatory terminal and placed close to the synaptic junction, the Ag filament formation dynamics can be modulated. For instance, during SET process (Figure 10d), increasing the amplitude of the positive voltage applied on the modulatory electrode can reduce the required pulse number for SET (Figure 10e), as a result of electric field enhancement near the filament tip. On the other hand, a negative bias voltage can suppress the electric field near the filament and effectively inhibit filament growth (Figure 10f). The bias voltage applied on the modulatory terminal was also found to affect the filament rupture process during RESET process (Figure 10g). Figure 10h and 10i show the postsynaptic current vs. applied RESET pulse number when negative and positive bias voltages were applied on the modulatory terminal. It was found that the filament rupture process was accelerated (suppressed) when a negative (positive) bias voltage was applied, which aided (impeded) the removal of Ag atoms from the filament.

Modulatory effects have also been explored in multi-terminal memristive systems based on van der Waals materials.^[53, 91] For example, a monolayer MoS_2 -based multi-terminal structure has been used to emulate a neural circuit, where the conductance of the MoS_2 film between two inner electrodes (as pre- and post- neurons) can be tuned by applying programming pulses on the two outer electrodes (as modulatory neurons). The effect is likely caused by the electric field (applied through the two modulatory electrodes) induced redistribution of defects in MoS_2 film, which act as dopants that modulate the Schottky barrier at the inner electrodes and change the synaptic weight.^[91]

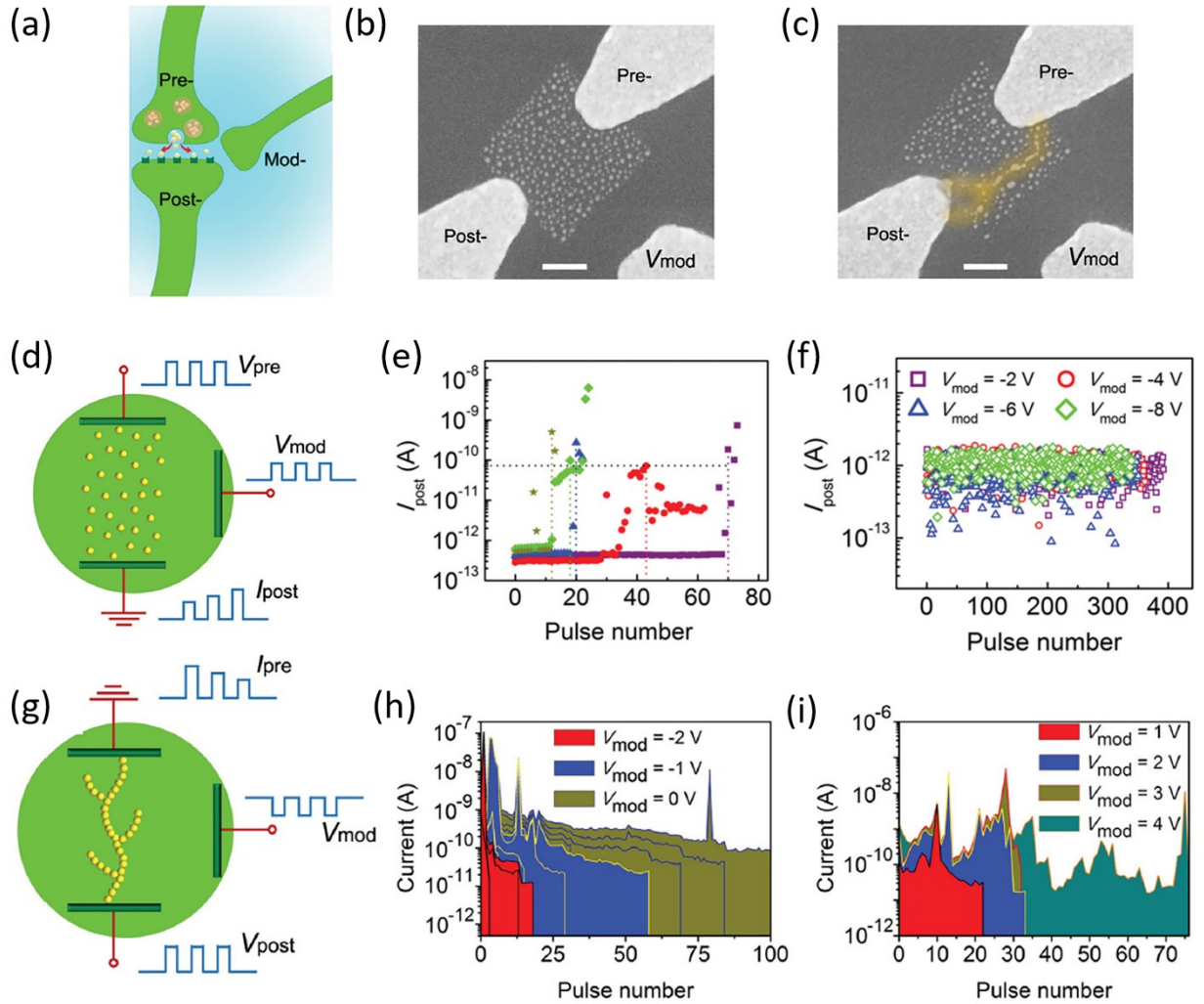


Figure 10. Implementing modulatory input-dependent plasticity. a) Schematic illustration of the setup. b–c) SEM images of the device at b) the pristine state, and c) after potentiation, where a Ag filament was formed between the presynaptic and postsynaptic terminals. Scale bar = 100 nm. d) Schematic illustration of the input and output signals in the heterosynaptic potentiation study. e, f) Postsynaptic current vs. applied V_{pre} pulse number, for e) different positive V_{mod} conditions ($V_{pre} = 10$ V, $V_{mod} = 0$ (square), 2 (circle), 4 (triangle), 6 (diamond), 8 V (star)), and f) different negative V_{mod} conditions ($V_{pre} = 10$ V, $V_{mod} = -2, -4, -6, -8$ V). g) Schematic illustration of the input and output signals in the heterosynaptic depression study. h, i) Current through the pre–post-terminal pair vs. the applied V_{post} pulse number, for h) different negative V_{mod} conditions ($V_{post} = 10$ V, $V_{mod} = 0, -1, -2$ V), and i) different positive V_{mod} conditions ($V_{post} = 10$ V, $V_{mod} = 1, 2, 3, 4$ V). Reproduced with permission.^[90] Copyright 2015, John Wiley & Sons, Inc.

Compared to the implementation of homosynaptic/heterosynaptic plasticity using digital circuits or software-based algorithms, these recent studies show that memristive systems can directly mimic the underlying ionic process in biology and enable diverse synaptic functions with low power and high integration density. Continued optimizations of the materials/devices and scaling

the prototype systems to larger networks will be the logical next step in the development of future neuromorphic computing systems.

4. Filament confinement to achieve improved uniformity

Due to the stochastic nature of ion migration, filaments can form randomly in the switching layer, possibly from different locations and with shapes during cycling, causing large cycle-cycle variations for parameters such as the switching voltage and the HRS/LRS resistances.^[84, 92] To improve the RS uniformity, approaches that can confine of the filament(s) at pre-defined, localized regions are desired. Recent studies suggest that precisely controlling the filaments and mitigate the device variations are indeed feasible, as discussed below.

4.1 Electrode engineering

The high electric field during SET/RESET is the main driving force that promotes the migration of ions, and the shape, size and growth direction of filaments are strongly dependent on the field distribution in the switching film. In an ideal, uniform device, the electric field should be uniformly distributed. However, factors such as film roughness can produce locally enhanced fields that facilitate the filament formation. To control the field distribution, methods aimed at engineering the electrode to induce controlled field enhancement at pre-defined locations have been proposed.

Introducing nanoclusters on the electrode of the RS device has been demonstrated to be useful in concentrating the electric field and confine the filaments. For example, in a Ag/ZrO₂/Pt RS device, Liu et al fabricated metal Cu nanoparticles on the bottom Pt electrode to concentrate the electric field.^[93] After switching the device to the LRS, Ag filaments formed at the positions of the Cu nanoparticles were visualized through TEM studies (**Figure 11a**). Further device characterizations show that compared to conventional devices (**Figure 11b**), SET/RESET voltage uniformity of the device with inserted Cu nanoparticles was apparently improved (**Figure 11c**), suggesting the localization of the Ag filament plays an important role in reducing the device variation. Instead of using metal nanoparticles, You et al fabricated Ni/NiO/Ti/Pt devices with insulating SiO_x nanodots formed at the interface between the Ti/Pt electrode and the NiO interface.^[94] TEM results revealed that a Ni filament was formed near the edge of the SiO_x nanodots (**Figure 11d-f**), due to the enhanced electric field there. The distribution of the SET/RESET voltage and the HRS/LRS resistance for 100 devices with and without SiO_x nanodots were compared, as shown in **Figures 11g and 11h**. It can be seen that the distributions of switching voltages and HRS/LRS resistances are significantly improved in devices with the SiO_x nanodots, supporting the hypothesis that controlled concentration of the electric field can improve RS uniformity.

An interesting alternative to localize the electric field is to use the thin edge of 2D materials, e.g. graphene, as the electrode (**Figure 11i**).^[95] Compared to nanoparticles that have a typical size of tens of nanometers, the thickness of the graphene edge is only a few angstroms and thus can more effectively concentrate the electric field and guide the filament formation (**Figure 11j**). When compared to control samples using the edge of a Pt film (~5 nm thick) as the electrode, improved switching voltage uniformity was observed (**Figure 11k**). In addition, the graphene electrode may

also act as a V_0 reservoir layer that actively participates in the RS process, resulting in a decrease in the switching voltage and the RESET current.

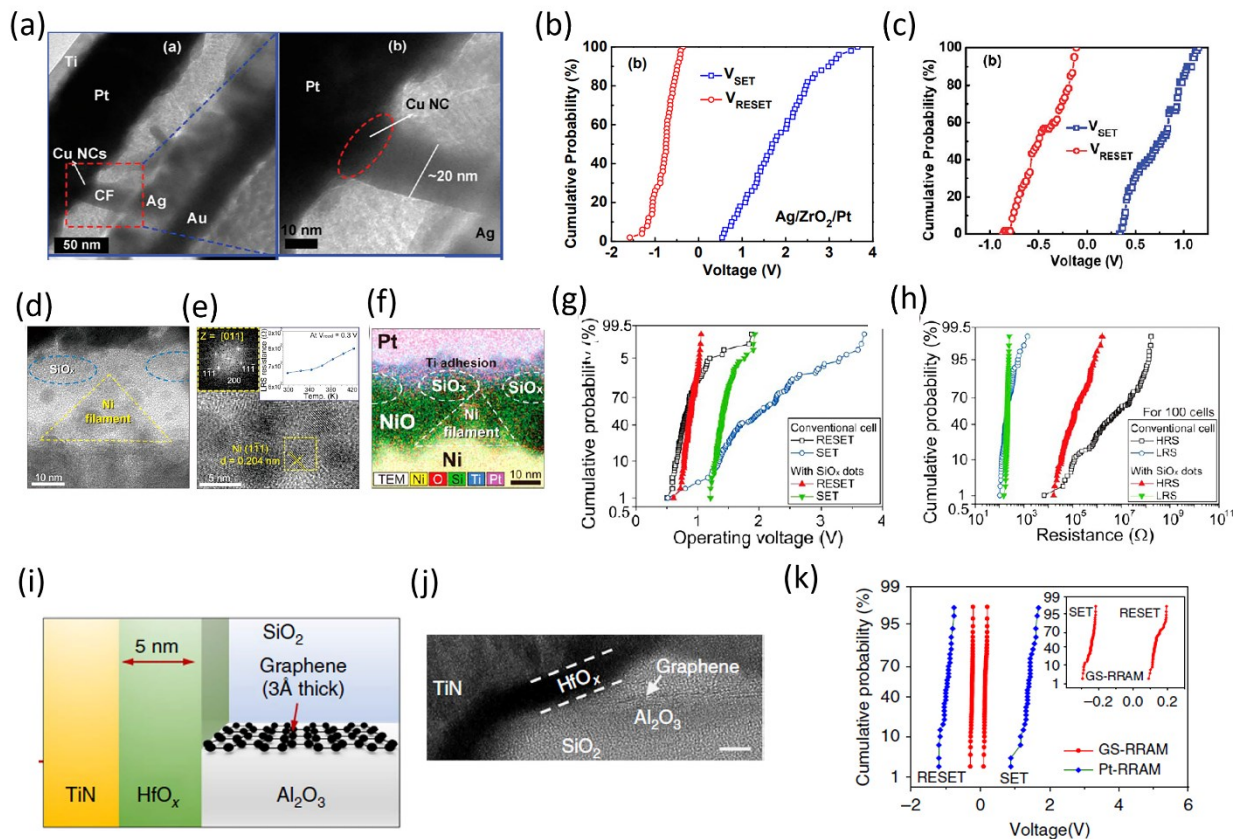


Figure 11. Improving device uniformity by concentrating the electric field. a) Left: Low-magnification cross-sectional TEM image of a Ag/ZrO₂/Cu nanocrystal/Pt memory cell after the SET process. Right: enlarged image of the red square region, showing the formation of a Ag filament on a Cu nanocrystal. b,c) Cell-to-cell cumulative distribution of the SET and RESET voltages in devices b) without and c) with the Cu nanocrystals. Reproduced with permission.^[93] Copyright 2010, American Chemical Society. d) TEM image of a NiO-based device having self-assembled SiO_x nanodots. The blue dotted circles represent the SiO_x nanodots, and the yellow dotted triangle indicates the Ni filament. e) HRTEM image showing Ni nanoparticles formed in the filament. The insets show the fast Fourier transform of the HRTEM image (left), and the temperature dependence of the LRS resistance which suggested metallic conduction LRS (right). f) EDS elemental mapping of Ni, O, Si, Ti and Pt in the device in LRS state. g,h) Cumulative probability graphs of the switching voltages (g) and the HRS/LRS resistances (h) for 100 memory cells with and without the SiO_x-nanodots. Reproduced with permission.^[94] Copyright 2014, American Chemical Society. i) Schematic cross-section of a device using HfO_x as the switching layer and TiN and graphene edge as the electrodes. j) HRTEM image of the device. k) The SET and RESET voltage distributions of GS-RRAM and Pt-RRAM after 50 cycles of switching. Reproduced with permission.^[95] Copyright 2015, Springer Nature.

4.2 Switching layer engineering

Beyond locally enhancing the field, variations in RS can be reduced by physically confining the ion migration path in the switching material. For example, Lee et al used engineered nanopores to confine and control the filament growth in a TaO_x based devices (**Figure 12a**).^[96] The authors inserted a graphene layer with pre-defined nanopores at the interface of the Ta₂O_{5-x}/TaO_y layers in a Pd/ Ta₂O_{5-x}/TaO_y/Pd device structure. The nanopores were created by e-beam lithography and oxygen plasma etching, with controlled locations and sizes down to 25 nm. As the graphene layer blocks the exchange of V_O between the Ta₂O_{5-x} switching layer and the TaO_y V_O reservoir layer, the filament growth can only be initiated at the nanopore region. The devices with the nanopores were shown to have a low switching current (Figure 12b) and a small standard deviation of the HRS/LRS read current (Figure 12c-d), indicating that the nanopore controls the V_O filament size and reduces the filament formation randomness.

The ion migration path can also be carefully controlled down to atomic scale by engineering the microstructure of switching material itself. For polycrystalline film-based RS devices, growth of filaments at the grain boundaries have been revealed by conductive atomic microscopy studies.^[97] The grain boundaries normally have high concentrations of defects and offer native paths for ion migration with a low activation energy. Therefore, by carefully designing the microstructure of the switching layer, it is possible to confine the filament formation and reduce the randomness. For example, Choi et al showed that the Ag filament formation can be confined to atomic-scale dislocations in epitaxially grown SiGe films and the switching parameter variations can be significantly reduced (Figure 12e-i).^[98] Since the dislocation is only a few nanometers in size, the Ag filament becomes deterministic during cycling. As a result, a very small variation (~1.7%) in the switching voltage can be obtained during SET process. Additionally, the size of the dislocation can be systematically controlled by using suitable etching conditions, allowing systematic tuning of the Ag filament size. This in turn leads to better control of the on/off ratio and multi-level resistance states that are desirable for neuromorphic computing applications.

Author Manuscript

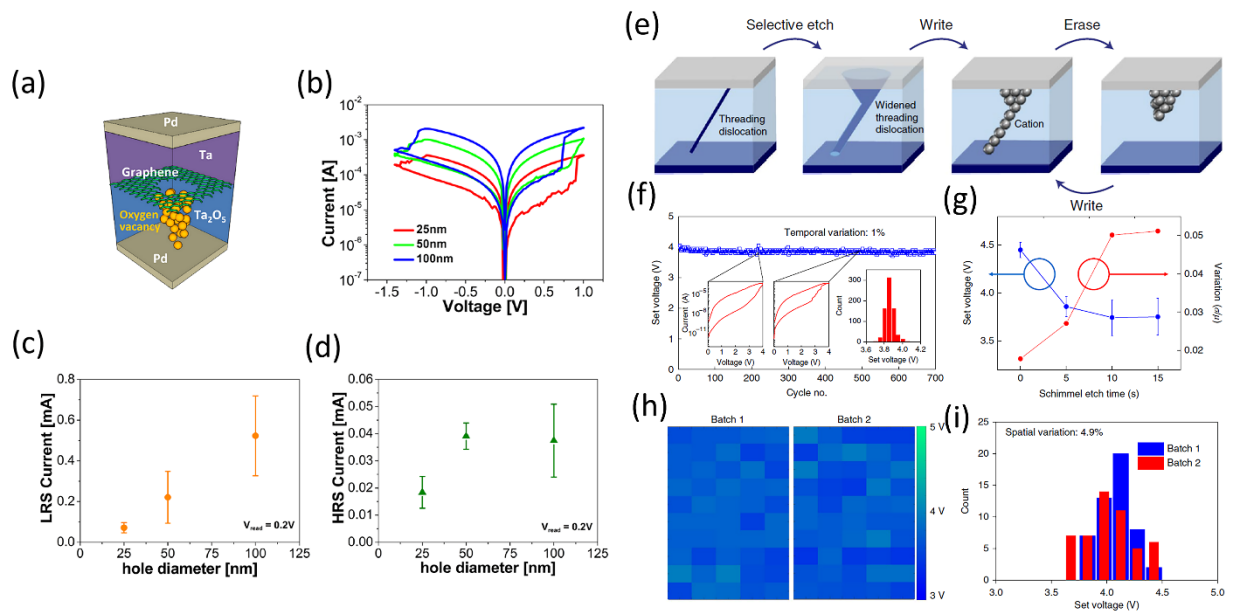


Figure 12. Improving device uniformity by confining the ion paths. a) Schematic of a graphene-inserted device structure, where oxygen ions can only transport through a nanopore created in the graphene layer. b) I - V characteristic of devices with different sized nanopores fabricated in the graphene layer, showing that the switching characteristics can be systematically tuned by the nanopores. c,d) Current levels in LRS (c) and HRS (d) of the graphene-inserted devices with different nanopore sizes. Reproduced with permission.^[96] Copyright 2016, American Chemical Society. e) Conceptual schematic showing filament formation confined to an engineered dislocation in epitaxial SiGe. f) SET voltage vs. cycle number during a cycling test. Insets: DC I - V plots at the 250th cycle and the 500th cycle, along with the histogram for the SET voltage distribution. g) Dependence of the SET voltage and its variation (σ/μ) on the defect-selective etch time. h) SET voltage plots overlaid with the optical micrographs for 50 devices in two different batches. i) Histograms for the SET voltage distribution shown in (h). Reproduced with permission.^[98] Copyright 2018, Springer Nature.

5. Reconfigurable nanostructures enabled by controlled ion migration at nanoscale

The ability to control the rearrangement of atoms/ions at the nanoscale in solid-state thin films, using simply an applied electric field, opens interesting opportunities to design and modulate material compositions and structures on the fly, in a reconfigurable fashion. Recent studies have confirmed this hypothesis and shown that these effects can be of importance for both fundamental researches that help understand coupled ionic/electronic behaviors at the atomic scale and for device designs and applications based on materials and structures that may not be achieved through conventional fabrication techniques alone.

5.1 Quantum point contacts (QPC)

By carefully controlling the programming conditions, filaments with widths of only a few atoms can be obtained in RS devices (**Figure 13a**). Consequently, the conductance of these atomic scale filaments becomes quantized as the channel size approaches the conduction electron Fermi wavelength and essentially forms a quantum point contact (QPC). The conductance of a QPC can be

expressed as $G=nG_0$ ($G_0=2e^2/h$), where n is an integer, e is the electron charge and h is the Planck's constant. Conductance quantization behavior has been observed in both cation and anion based RS devices.^[99-102]

Figure 13b shows the conductance of a Nb/ZnO/Pt device as a function of the bias voltage during SET process, where discrete increases in the device conductance by multiples of G_0 can be clearly observed. Such QPC structures can naturally lead to multilevel storage for high-density memory applications due to the fundamental, discrete conductance changes. In addition, the controlled QPC formation also offers a platform to study the electrical properties of one-dimensional nanostructures. For example, an interesting observation is the half-integer multiples of G_0 observed in many RS devices after the formation of atom-sized filament. The half-integer values may originate from the imperfect atom configuration^[103] at the QPC, or impurity atoms from the switching layer^[99]. RS devices allow these interesting phenomena to be studied in materials that were not available before, and can help deepen our understanding of electrical transport in low-dimensional nanostructures and develop circuit concepts based on these quantum effects.

5.2 Selector devices

Selector devices with high non-linearity are desirable for high-density memory applications, since they can potentially be integrated with RS memory elements in a passive crossbar structure, without the need of active components such as transistors.^[104] It has been shown that in volatile memristors^[105-106] (e.g. Ag/HfO₂/Ag), weak Ag filaments with short retention are formed during programming and spontaneously regroup into discrete Ag nanoparticles after field removal, allowing the device to show threshold switching behaviors^[107]. These devices offer steep turn-on of <1 mV dec⁻¹ and high on/off ratio of 10^{10} , which can effectively suppress the leakage current in passive crossbar arrays. Similarly, Xue et al demonstrated that by driving oxygen ions in V₂O₅ under an electric field, monoclinic VO₂ nanofilaments with sizes of a few nanometers can be formed (Figure 13c).^[108] This process corresponds to a metal-insulator transition behavior and can be employed to build selector devices with steep turn-on (<0.5 mV/dec) and low variations ($<4.3\%$) (Figure 13d). By serially connecting these selector devices with nonvolatile RS elements, the resulting 1S1R structure shows good performance in suppressing sneak currents in the crossbar array.

5.3 Radiofrequency switches

High-performance radiofrequency (RF) switches that can be scaled down to nanoscale are desirable for integrating high-density RF and wireless components with logic and other electronic components. Pi et al fabricated a planar memristive device consisting of a pair of Ag and Au electrodes separated by a small air gap (~ 35 nm).^[109] By electrically controlling the formation (Figure 13e) and rupture (Figure 13f) of a Ag filament in the air gap, the device can be turned on and off with a resistance ratio up to 10^{12} . This device shows excellent RF performances, such as low insertion loss (0.33 dB at 40 GHz) at on state (Figure 13g) and high isolation (30 dB at 40 GHz) at off state (Figure 13h), along with a high cutoff frequency of 35 THz.

5.4 Magnetic nanostructures

Beyond resistance changes, the ability to re-arrange ions opens up many other interesting possibilities. For example, controlling the migration of ferromagnetic metal ions/atoms in a dielectric layer makes it possible to fabricate interesting magnetic devices, whose magnetic properties can be tuned on the fly by an applied electric field. One typical example is the magnetic tunneling junction (MTJ), which consists of a thin tunneling layer sandwiched between two ferromagnetic metal electrodes. Such a device can show tunnel magnetoresistance (TMR) effects with a high (low) resistance if the magnetization directions of the two ferromagnetic electrodes are parallel (antiparallel). Yang et al showed that in a Co/ZnO/Fe sandwich structure, by carefully controlling the growth of a Co filament in the ZnO film, the thickness of the ZnO insulating layer between the Co filament (which acts as an extension of the Co electrode) and the Fe electrode can be precisely controlled, as shown in Figure 13i. When the ZnO film is thin enough to serve as an electron tunneling layer, TMR effect can be observed from the electrically-controlled formation of MTJs (Figure 13j).^[110]

Additionally, the controlled ion migration also enables direct modulation of the local magnetic domain structures in magnetic thin films.^[26, 111-112] For instance, in $\text{LiFe}_5\text{O}_{8-x}$ films it was shown that removing Li^+ ions from the film during the SET process increases the valence state of the Fe ions, which can lead to an increase of the local magnetization intensity and the growth of the magnetic domains.^[26] Magnetic domain wall motion, driven by the expansion of the magnetic domains, was further observed for distances over 100 nm. These magneto-ionic effects, obtained through directly modulating the material composition, offer a new approach to design and operate magnetic structures at the nanoscale.

5.5 Water permeation membranes

Controlling the permeation rate of water molecules through a membrane is critical as it can lead to applications such as water purification. Recently, Zhou et al showed that, in a graphene oxide (GO) membrane (Figure 13k) applying an electric field can create local and conductive filaments (Figure 13l) that are rich of carbon.^[113] Afterwards, the flow rate of water molecules through the GO membrane can be precisely controlled by tuning the device current, as shown in Figure 13m. It is likely that the high-density current flow through the filaments creates a high electric field which ionizes water molecules and leads to the formation H_3O^+ and OH^- clusters that can impede the water transport. The controlled water permeation may in turn lead to a variety of smart membrane applications such as advanced nanofluidic devices.

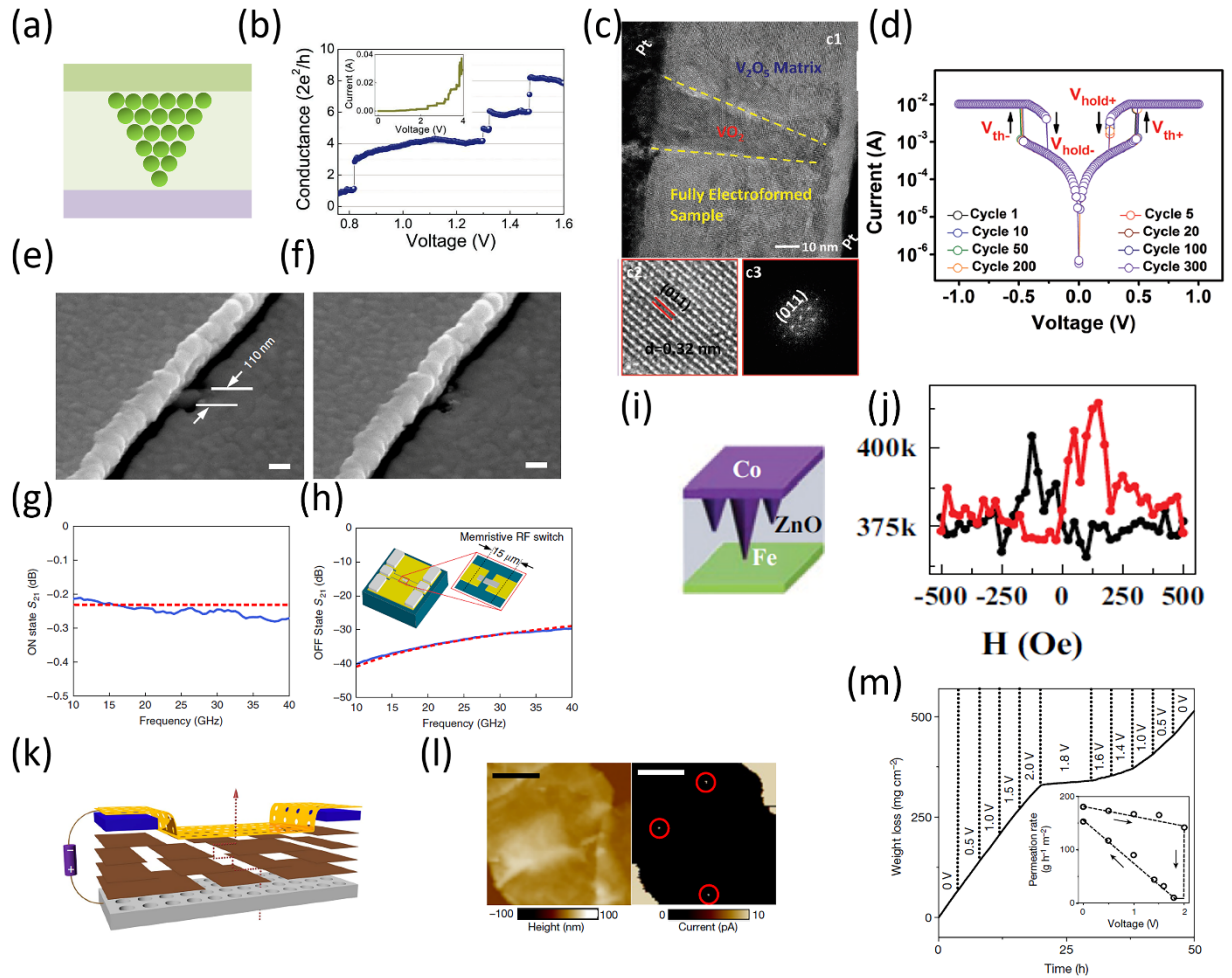


Figure 13. Novel nanoionic devices realized by electric-field-controlled ion migration. a) Schematic of a quantum-point contact formed in a RS device. b) Measured conductance as a function of the bias voltage during SET process in a Nb/ZnO/Pt device. Discrete increase of conductance by multiples of the quantum conductance (G_0) is clearly visible. Reproduced with permission.^[99] Copyright 2012, John Wiley & Sons, Inc. c) Cross-sectional HRTEM images and fast Fourier transformed images showing a VO_2 nanochannel formed in a V_2O_5 -based device. d) Threshold-switching characteristics of the V_2O_5 -based RS device for over 300 consecutive cycles. Reproduced with permission.^[108] Copyright 2017, John Wiley & Sons, Inc. e) SEM image showing a Ag filament connecting the Ag and Au metal electrodes. f) In the OFF state, the filament in (e) is ruptured, leaving a gap between the two electrodes. Scale bars, 100 nm. g-h) Typical transmission spectrum (solid blue line) and simulation results (dashed red line) of a device at the ON state (g) and the OFF state (h). The insertion loss is lower than 0.3 dB at the ON state and 30 dB at the OFF state at 40 GHz. Reproduced with permission.^[109] Copyright 2015, Springer Nature. i) Schematic of a Co/ZnO/Fe device with a partially formed Co conductive filament. j) Resistance as a function of the magnetic field in a Co/ZnO/Fe device with partially formed Co filaments, showing typical magnetoresistance curves. Reproduced with permission.^[110] Copyright 2014, EPLA. k) Schematic of a graphene oxide membrane deposited on a porous silver substrate, with an applied bias voltage. The dotted line shows a possible pathway for water permeation. l) Topography (left) and the corresponding current image (right) of such a graphene oxide membrane after filament formation. The conducting filaments (size ranging from 20 to 45 nm) formed in the graphene oxide membrane are marked by red circles. Scale

bars, 1 μm . m) Weight loss for a water-filled container sealed with a 1- μm -thick graphene oxide membrane (7-mm diameter), for cases with different voltages applied across the membrane during the filament formation process. Inset: water permeation rate through the graphene oxide membrane as a function of applied voltage, showing the apparent decrease of the permeation rate after the device was switched to the LRS at ≈ 2 V. Reproduced with permission.^[113] Copyright 2018, Springer Nature.

6. Conclusions and Outlook

In this review, we discussed ion migration induced RS effects in solid-state films and how these nanoionic devices may be used for a broad range of applications. We showed that at high fields, a broad range of cations (e.g. Ag^+ , Pd^{2+} , Li^+ and H^+) and anions (e.g. O^{2-} , I^- and S^{2-}) can be redistributed, which either creates metallic intrusions or changes the film's local stoichiometry. These ionic processes thus directly change the film's chemical composition and its physical properties such as the local resistivity, leading to RS effects. From a theoretical point of view, the rich ionic dynamics at the nanoscale provide state variables that can evolve at different time scales, which enables natural implementation of important biological functions. These properties make the memristor system a promising candidate for hardware implementation of neuromorphic computing systems.

Several strategies to control the ionic processes have been presented, including local electric field enhancement and ion migration path confinement. They have been shown to be effective in reducing the randomness during filament formation and improving device performance and uniformity. Other applications based on controlled ion migration beyond memory and neuromorphic computing have also been discussed, including RF switches for wireless communication, magnetic sensors and water purification.

Despite the tremendous progress that has been made, our understanding of the dynamic ion process during RS is far from complete. The specific roles of potential driving forces including electric field, chemical potential gradient and Joule heat, as well as other factors such as stress during the RS process is not quantitatively understood. The actual process is likely complex in these seemingly simple two-terminal devices, affected by a combination of the different kinetic and thermodynamic factors. Efforts to acquire such knowledge will not only provide guidelines to engineer better device configuration or material properties to optimize device performance, but will also help explore more efficient, bio-inspired information processing approaches in the solid-state devices and circuits for current and future computing applications.

To facilitate large-scale device applications, continued improvements on the ionic process control are required to address the device variation issue. Confining the ion migration channels at the atomic scale is a promising approach, where the redistribution of only a few ions/atoms is needed^[96]. Better control also brings additional benefits including improved device scalability and reduced power consumption. Beyond RS effects, the ability to directly modulate the composition of nanostructures through controlled ion redistribution offers new and exciting opportunities for the design and applications of electronic, magnetic, optical and energy devices with interesting physiochemical properties and reconfigurable functionalities.

Acknowledgement

The authors would like to thank Dr. J. Lee and Dr. Y. Jeong for helpful and stimulating discussions, and the financial support by the National Science Foundation (NSF) through grants ECCS-1708700 and DMR-1810119.

References

- [1] J. Maier, *Nat. Mater.* **2005**, *4*, 805.
- [2] R. Waser, R. Dittmann, G. Staikov, K. Szot, *Adv. Mater.* **2009**, 2632-2663.
- [3] L. Chua, *IEEE Trans. On Circuit Theory* **1971**, *18*, 507-519.
- [4] D. B. Strukov, G. S. Snider, D. R. Stewart, R. S. Williams, *Nature* **2008**, *453*, 80.
- [5] R. Waser, M. Aono, *Nat. Mater.* **2007**, *6*, 833.
- [6] B. J. Choi, A. C. Torrezan, J. P. Strachan, P. G. Kotula, A. J. Lohn, M. J. Marinella, Z. Li, R. S. Williams, J. J. Yang, *Adv. Funct. Mater.* **2016**, *26*, 5290-5296.
- [7] Z. Wei, Y. Kanzawa, K. Arita, Y. Katoh, K. Kawai, S. Muraoka, S. Mitani, S. Fujii, K. Katayama, M. Iijima, T. Mikawa, T. Ninomiya, R. Miyanaga, Y. Kawashima, K. Tsuji, A. Himeno, T. Okada, R. Azuma, K. Shimakawa, H. Sugaya, T. Takagi, R. Yasuhara, K. Horiba, H. Kumigashira, M. Oshima, *IEDM* **2008**, 1-4.
- [8] M.-J. Lee, C. B. Lee, D. Lee, S. R. Lee, M. Chang, J. H. Hur, Y.-B. Kim, C.-J. Kim, D. H. Seo, S. Seo, U. I. Chung, I.-K. Yoo, K. Kim, *Nat. Mater.* **2011**, *10*, 625.
- [9] S. Pi, C. Li, H. Jiang, W. Xia, H. Xin, J. J. Yang, Q. Xia, *Nat. Nanotechnol.* **2019**, *14*, 35-39.
- [10] J. Lee, W. D. Lu, *Adv. Mater.* **2018**, *30*, 1702770.
- [11] M. A. Zidan, J. P. Strachan, W. D. Lu, *Nat. Electron.* **2018**, *1*, 22-29.
- [12] Z. Wang, L. Wang, M. Nagai, L. Xie, M. Yi, W. Huang, *Adv. Electron. Mater.* **2017**, *3*, 1600510.
- [13] S. G. Kim, J. S. Han, H. Kim, S. Y. Kim, H. W. Jang, *Adv. Mater. Technol.* **2018**, *3*, 1800457.
- [14] C. Gu, J. S. Lee, *ACS Nano*, **2016**, *10*, 5413-5418.
- [15] Y. Li, S. Long, Q. Liu, H. Lv, M. Liu, *Small* **2017**, *13*, 1604306.
- [16] Y. Yang, P. Gao, S. Gaba, T. Chang, X. Pan, W. Lu, *Nat. Commun.* **2012**, *3*, 732.
- [17] Y. Yang, P. Gao, L. Li, X. Pan, S. Tappertzhofen, S. Choi, R. Waser, I. Valov, W. D. Lu, *Nat. Commun.* **2014**, *5*, 4232.
- [18] I. Valov, R. Waser, J. R. Jameson, M. N. Kozicki, *Nanotechnology* **2011**, *22*, 254003.
- [19] M. N. Kozicki, H. J. Barnaby, *Semicond. Sci. Technol.* **2016**, *31*, 113001.
- [20] M. Kund, G. Beitel, C.-U. Pinnow, T. Rohr, J. Schumann, R. Symanczyk, K. Ufert, G. Muller, *IEDM* **2005**, 754-757.
- [21] Z. Wang, H. Jiang, M. H. Jang, P. Lin, A. Ribbe, Q. Xia, J. J. Yang, *Nanoscale* **2016**, *8*, 14023-14030.
- [22] Y. Shao-Horn, L. Croguennec, C. Delmas, E. C. Nelson, M. A. O'Keefe, *Nat. Mater.* **2003**, *2*, 464.
- [23] A. Van der Ven, G. Ceder, *J. Power Sources* **2001**, *97*, 529-531.
- [24] V. S. Nguyen, V. H. Mai, P. Auban Senzier, C. Pasquier, K. Wang, M. J. Rozenberg, N. Brun, K. March, F. Jomard, J. Giapintzakis, Van Son Nguyen Van Huy Mai Pascale AubC. N. Mihailescu, E. Kyriakides, P. Nukala, T. Maroutian, G. Agnus, P. Lecoeur, S. Matzen, P. Aubert, S. Franger, R. Salot, P. - A. Albouy, D. Alamarguy, B. Dkhil, P. Chrétien, O. Schneegans, *Small* **2018**, *14*, 1801038.
- [25] X. Zhu, C. S. Ong, X. Xu, B. Hu, J. Shang, H. Yang, S. Katlakunta, Y. Liu, X. Chen, L. Pan, J. Ding, R.-W. Li, *Sci. Rep.* **2013**, *3*, 1084.
- [26] X. Zhu, J. Zhou, L. Chen, S. Guo, G. Liu, R. W. Li, W. D. Lu, *Adv. Mater.* **2016**, *28*, 7658-7665.
- [27] A. Hanada, K. Kinoshita, S. Kishida, *Appl. Phys. Lett.* **2012**, *101*, 043507.
- [28] Y. Zhou, Y. Peng, Y. Yin, F. Zhou, C. Liu, J. Ling, L. Lei, W. Zhou, D. Tang, *Sci. Rep.* **2016**, *6*, 32712.

- [29] J. J. Yang, D. B. Strukov, D. R. Stewart, *Nat. Nanotechnol.* **2013**, *8*, 13.
- [30] J. J. Yang, M. D. Pickett, X. Li, D. A. Ohlberg, D. R. Stewart, R. S. Williams, *Nat. Nanotechnol.* **2008**, *3*, 429.
- [31] J. J. Yang, F. Miao, M. D. Pickett, D. A. Ohlberg, D. R. Stewart, C. N. Lau, R. S. Williams, *Nanotechnology* **2009**, *20*, 215201.
- [32] D.-H. Kwon, K. M. Kim, J. H. Jang, J. M. Jeon, M. H. Lee, G. H. Kim, X.-S. Li, G.-S. Park, B. Lee, S. Han, *Nat. Nanotechnol.* **2010**, *5*, 148.
- [33] F. Miao, J. P. Strachan, J. J. Yang, M. X. Zhang, I. Goldfarb, A. C. Torrezan, P. Eschbach, R. D. Kelley, G. Medeiros - Ribeiro, R. S. Williams, *Adv. Mater.* **2011**, *23*, 5633-5640.
- [34] S. Kim, S.-J. Kim, K. M. Kim, S. R. Lee, M. Chang, E. Cho, Y.-B. Kim, C. J. Kim, U. In Chung, I.-K. Yoo, *Sci. Rep.* **2013**, *3*, 1680.
- [35] S. Menzel, U. Böttger, M. Wimmer, M. Salinga, *Adv. Funct. Mater.* **2015**, *25*, 6306-6325.
- [36] S. Kumar, C. E. Graves, J. P. Strachan, E. M. Grafals, A. L. D. Kilcoyne, T. Tyliczszak, J. N. Weker, Y. Nishi, R. S. Williams, *Adv. Mater.* **2016**, *28*, 2772-2776.
- [37] A. S. Alexandrov, A. M. Bratkovsky, B. Bridle, S. E. Savel'ev, D. B. Strukov, R. S. Williams, *Appl. Phys. Lett.* **2011**, *99*, 202104.
- [38] S. Slesazeck, H. Mähne, H. Wylezich, A. Wachowiak, J. Radhakrishnan, A. Ascoli, R. Tetzlaff, T. Mikolajick, *RSC Adv.* **2015**, *5*, 102318-102322.
- [39] G. A. Gibson, S. Musunuru, J. Zhang, K. Vandenberghe, J. Lee, C.-C. Hsieh, W. Jackson, Y. Jeon, D. Henze, Z. Li, R. S. Williams, *Appl. Phys. Lett.* **2016**, *108*, 023505.
- [40] J. M. Goodwill, A. A. Sharma, D. Li, J. A. Bain, M. Skowronski, *ACS Appl. Mater. Interfaces* **2017**, *9*, 11704-11710.
- [41] Z. Wang, M. Yin, T. Zhang, Y. Cai, Y. Wang, Y. Yang, R. Huang, *Nanoscale* **2016**, *8*, 14015-14022.
- [42] S. Kim, S. Choi, W. Lu, *ACS Nano* **2014**, *8*, 2369-2376.
- [43] I. Goldfarb, F. Miao, J. J. Yang, W. Yi, J. Strachan, M.-X. Zhang, M. Pickett, G. Medeiros-Ribeiro, R. S. Williams, *Appl. Phys. A* **2012**, *107*, 1-11.
- [44] B. Hwang, J. S. Lee, *Adv. Electron. Mater.* **2018**, *5*, 1800519.
- [45] M. A. Green, A. Ho-Baillie, H. J. Snaith, *Nat. Photon.* **2014**, *8*, 506.
- [46] L. Dou, Y. Yang, J. You, Z. Hong, W.-H. Chang, G. Li, Y. Yang, *Nat. Commun.* **2014**, *5*, 5404.
- [47] H. Cho, S.-H. Jeong, M.-H. Park, Y.-H. Kim, C. Wolf, C.-L. Lee, J. H. Heo, A. Sadhanala, N. Myoung, S. Yoo, *Science* **2015**, *350*, 1222-1225.
- [48] H. Zhu, Y. Fu, F. Meng, X. Wu, Z. Gong, Q. Ding, M. V. Gustafsson, M. T. Trinh, S. Jin, X. Zhu, *Nat. Mater.* **2015**, *14*, 636.
- [49] X. Zhu, J. Lee, W. D. Lu, *Adv. Mater.* **2017**, *29*, 1700527.
- [50] P. Cheng, K. Sun, Y. H. Hu, *Nano Lett.* **2016**, *16*, 572-576.
- [51] A. A. Bessonov, M. N. Kirikova, D. I. Petukhov, M. Allen, T. Ryhänen, M. J. A. Bailey, *Nat. Mater.* **2014**, *14*, 199.
- [52] V. K. Sangwan, D. Jariwala, I. S. Kim, K.-S. Chen, T. J. Marks, L. J. Lauhon, M. C. Hersam, *Nat. Nanotechnol.* **2015**, *10*, 403.
- [53] D. Li, B. Wu, X. Zhu, J. Wang, B. Ryu, W. D. Lu, W. Lu, X. Liang, *ACS Nano* **2018**, *12*, 9240-9252.
- [54] A. Wedig, M. Luebben, D.-Y. Cho, M. Moors, K. Skaja, V. Rana, T. Hasegawa, K. K. Adepalli, B. Yildiz, R. Waser, *Nat. Nanotechnol.* **2016**, *11*, 67.
- [55] H. Jiang, L. Han, P. Lin, Z. Wang, M. H. Jang, Q. Wu, M. Barnell, J. J. Yang, H. L. Xin, Q. Xia, *Sci. Rep.* **2016**, *6*, 28525.
- [56] J. J. Hopfield, *Nature* **1995**, *376*, 33.
- [57] G.-q. Bi, M.-m. Poo, *J. Neurosci.* **1998**, *18*, 10464-10472.
- [58] L. F. Abbott, S. B. Nelson, *Nat. Neurosci.* **2000**, *3*, 1178.
- [59] S. H. Jo, T. Chang, I. Ebong, B. B. Bhadviya, P. Mazumder, W. Lu, *Nano Lett.* **2010**, *10*, 1297-1301.
- [60] B. P. Bean, *Nat. Rev. Neurosci.* **2007**, *8*, 451.

- [61] H. Kamiya, R. S. Zucker, *Nature* **1994**, *371*, 603.
- [62] N. Unwin, *Cell* **1993**, *72*, 31-41.
- [63] J. G. G. Borst, B. Sakmann, *Nature* **1996**, *383*, 431-434.
- [64] D. S. Jeong, K. M. Kim, S. Kim, B. J. Choi, C. S. Hwang, *Adv. Electron. Mater.* **2016**, *2*, 1600090.
- [65] R. S. Zucker, W. G. Regehr, *Annu. Rev. Physiol.* **2002**, *64*, 355-405.
- [66] T. Chang, S.-H. Jo, W. Lu, *ACS Nano* **2011**, *5*, 7669-7676.
- [67] M. F. Bear, R. C. Malenka, *Curr. Opin. Neurobiol.* **1994**, *4*, 389-399.
- [68] T. V. Bliss, G. L. Collingridge, *Nature* **1993**, *361*, 31.
- [69] T. Ohno, T. Hasegawa, T. Tsuruoka, K. Terabe, J. K. Gimzewski, M. Aono, *Nat. Mater.* **2011**, *10*, 591.
- [70] X. Yan, J. Zhao, S. Liu, Z. Zhou, Q. Liu, J. Chen, X. Y. Liu, *Adv. Funct. Mater.* **2018**, *28*, 1705320.
- [71] S. Kim, C. Du, P. Sheridan, W. Ma, S. Choi, W. D. Lu, *Nano Lett.* **2015**, *15*, 2203-2211.
- [72] C. Du, W. Ma, T. Chang, P. Sheridan, W. D. Lu, *Adv. Funct. Mater.* **2015**, *25*, 4290-4299.
- [73] Z. Wang, S. Joshi, S. E. Savel'ev, H. Jiang, R. Midya, P. Lin, M. Hu, N. Ge, J. P. Strachan, Z. Li, Q. Wu, M. Barnell, G.-L. Li, H. L. Xin, R. Stanley Williams, Q. Xia, J. J. Yang, *Nat. Mater.* **2017**, *16*, 101.
- [74] X. Zhu, C. Du, Y. Jeong, W. D. Lu, *Nanoscale* **2017**, *9*, 45-51.
- [75] Z. H. Tan, R. Yang, K. Terabe, X. B. Yin, X. D. Zhang, X. Guo, *Adv. Mater.* **2016**, *28*, 377-384.
- [76] Q. Wu, H. Wang, Q. Luo, W. Banerjee, J. Cao, X. Zhang, F. Wu, Q. Liu, L. Li, M. Liu, *Nanoscale* **2018**, *10*, 5875-5881.
- [77] C. Cheng, Y. Li, T. Zhang, Y. Fang, J. Zhu, K. Liu, L. Xu, Y. Cai, X. Yan, Y. Yang, *J. Appl. Phys.* **2018**, *124*, 152103.
- [78] L. O. Chua, S. M. Kang, *Proc. IEEE.* **1976**, *64*, 209-223.
- [79] T. Chang, S.-H. Jo, K.-H. Kim, P. Sheridan, S. Gaba, W. Lu, *Appl. Phys. A* **2011**, *102*, 857-863.
- [80] M. A. Zidan, Y. Jeong, W. D. Lu, *IEEE Trans. on Nanotechnol.* **2017**, *16*, 721-723.
- [81] R. Yang, H.-M. Huang, Q.-H. Hong, X.-B. Yin, Z.-H. Tan, T. Shi, Y.-X. Zhou, X.-S. Miao, X.-P. Wang, S.-B. Mi, C.-L. Jia, X. Guo, *Adv. Funct. Mater.* **2018**, *28*, 1704455.
- [82] S. Song, K. D. Miller, L. F. Abbott, *Nat. Neurosci.* **2000**, *3*, 919.
- [83] W. C. Abraham, M. F. Bear, *Trends Neurosci.* **1996**, *19*, 126-130.
- [84] S. Menzel, P. Kaupmann, R. Waser, *Nanoscale* **2015**, *7*, 12673-12681.
- [85] F. Pan, S. Yin, V. Subramanian, *Electron Device. Lett.* **2011**, *32*, 949-951.
- [86] M. J. Berridge, P. Lipp, M. D. Bootman, *Nat. Rev. Mol. Cell Bio.* **2000**, *1*, 11.
- [87] R. Fonseca, In *Synaptic Tagging and Capture*, **2015**, 29-44 (Springer, New York).
- [88] X. Zhu, D. Li, X. Liang, W. D. Lu, *Nat. Mater.* **2019**, *18*, 141-148.
- [89] C. H. Bailey, M. Giustetto, Y.-Y. Huang, R. D. Hawkins, E. R. Kandel, *Nat. Rev. Neurosci.* **2000**, *1*, 11.
- [90] Y. Yang, B. Chen, W. D. Lu, *Adv. Mater.* **2015**, *27*, 7720-7727.
- [91] V. K. Sangwan, H.-S. Lee, H. Bergeron, I. Balla, M. E. Beck, K.-S. Chen, M. C. Hersam, *Nature* **2018**, *554*, 500.
- [92] S. Qin, Z. Liu, G. Zhang, J. Zhang, Y. Sun, H. Wu, H. Qian, Z. Yu, *Phys. Chem. Chem. Phys.* **2015**, *17*, 8627-8632.
- [93] Q. Liu, S. Long, H. Lv, W. Wang, J. Niu, Z. Huo, J. Chen, M. Liu, *ACS Nano* **2010**, *4*, 6162-6168.
- [94] B. K. You, W. I. Park, J. M. Kim, K.-I. Park, H. K. Seo, J. Y. Lee, Y. S. Jung, K. J. Lee, *ACS Nano* **2014**, *8*, 9492-9502.
- [95] S. Lee, J. Sohn, Z. Jiang, H.-Y. Chen, H.-S. P. Wong, *Nat. Commun.* **2015**, *6*, 8407.
- [96] J. Lee, C. Du, K. Sun, E. Kioupakis, W. D. Lu, *ACS Nano* **2016**, *10*, 3571-3579.
- [97] M. Lanza, K. Zhang, M. Porti, M. Nafria, Z. Shen, L. Liu, J. Kang, D. Gilmer, G. Bersuker, *Appl. Phys. Lett.* **2012**, *100*, 123508.
- [98] S. Choi, S. H. Tan, Z. Li, Y. Kim, C. Choi, P.-Y. Chen, H. Yeon, S. Yu, J. Kim, *Nat. Mater.* **2018**, *17*, 335.

- [99] X. Zhu, W. Su, Y. Liu, B. Hu, L. Pan, W. Lu, J. Zhang, R. W. Li, *Adv. Mater.* **2012**, *24*, 3941-3946.
- [100] S. Long, X. Lian, C. Cagli, X. Cartoixa, R. Rurali, E. Miranda, D. Jiménez, L. Perniola, M. Liu, J. Suné, *Appl. Phys. Lett.* **2013**, *102*, 183505.
- [101] A. Mehonic, A. Vrajitoarea, S. Cuff, S. Hudziak, H. Howe, C. Labbe, R. Rizk, M. Pepper, A. Kenyon, *Sci. Rep.* **2013**, *3*, 2708.
- [102] S. R. Nandakumar, M. Minvielle, S. Nagar, C. Dubourdieu, B. Rajendran, *Nano Lett.* **2016**, *16*, 1602-1608.
- [103] K. Krishnan, M. Muruganathan, T. Tsuruoka, H. Mizuta, M. Aono, *Adv. Funct. Mater.* **2017**, *27*, 1605104.
- [104] R. Aluguri, T. Tseng, *IEEE J. Electron Devices Soc.* **2016**, *4*, 294-306.
- [105] Z. Wang, M. Rao, R. Midya, S. Joshi, H. Jiang, P. Lin, W. Song, S. Asapu, Y. Zhuo, C. Li, H. Wu, Q. Xia, J. J. Yang, *Adv. Funct. Mater.* **2018**, *28*, 1704862.
- [106] Z. Wang, S. Joshi, S. E. Savel'ev, H. Jiang, R. Midya, P. Lin, M. Hu, N. Ge, J. P. Strachan, Z. Li, Q. Wu, M. Barnell, G. L. Li, H. L. Xin, R. S. Williams, Q. Xia, J. J. Yang, *Nat. Mater.* **2016**, *16*, 101.
- [107] R. Midya, Z. Wang, J. Zhang, S. E. Savel'ev, C. Li, M. Rao, M. H. Jang, S. Joshi, H. Jiang, P. Lin, K. Norris, N. Ge, Q. Wu, M. Barnell, Z. Li, H. L. Xin, R. S. Williams, Q. Xia, J. J. Yang, *Adv. Mater.* **2017**, *29*, 1604457.
- [108] W. Xue, G. Liu, Z. Zhong, Y. Dai, J. Shang, Y. Liu, H. Yang, X. Yi, H. Tan, L. Pan, S. Gao, J. Ding, X.-H. Xu, R.-W. Li, *Adv. Mater.* **2017**, *29*, 1702162.
- [109] S. Pi, M. Ghadiri-Sadrabadi, J. C. Bardin, Q. Xia, *Nat. Commun.* **2015**, *6*, 7519.
- [110] Z. Yang, Q. Zhan, X. Zhu, Y. Liu, H. Yang, B. Hu, J. Shang, L. Pan, B. Chen, R.-W. Li, *EPL* **2014**, *108*, 58004.
- [111] X. Chen, X. Zhu, W. Xiao, G. Liu, Y. P. Feng, J. Ding, R.-W. Li, *ACS Nano* **2015**, *9*, 4210-4218.
- [112] A. J. Tan, M. Huang, C. O. Avci, F. Büttner, M. Mann, W. Hu, C. Mazzoli, S. Wilkins, H. L. Tuller, G. S. D. Beach, *Nat. Mater.* **2019**, *18*, 35-41.
- [113] K.-G. Zhou, K. Vasu, C. Cherian, M. Neek-Amal, J. C. Zhang, H. Ghorbanfekr-Kalashami, K. Huang, O. Marshall, V. Kravets, J. Abraham, *Nature* **2018**, *559*, 236.



Xiaojian Zhu is currently a postdoctoral research fellow in the Electrical Engineering and Computer Science department of the University of Michigan. He received a Ph.D. in material science from Ningbo Institute of Materials Technology and Engineering (NIMTE), Chinese Academy of Sciences (CAS) in 2014. His research interests includes ionic memristor devices for neuromorphic computing and novel solid-state functional devices based on nanoionic effects.



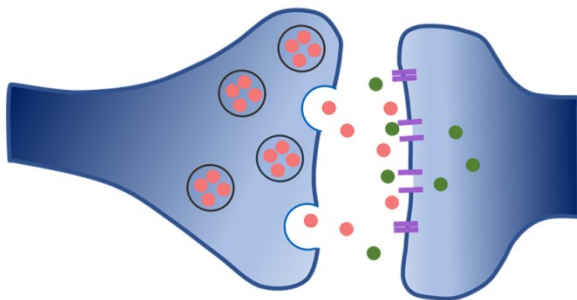
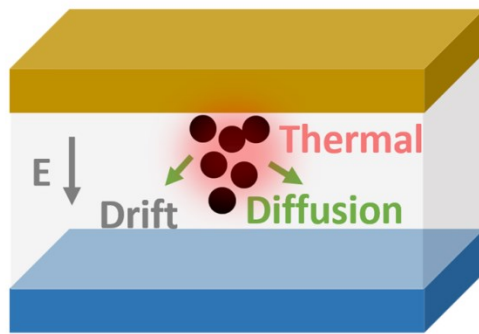
Seung hwan Lee received a B.S. and an M.S in physics and applied physics from Osaka University, Japan, in 2006 and 2008, respectively. He is currently pursuing a Ph.D. degree at the University of Michigan. His research interests include emerging devices (ReRAM, PCRAM, and MRAM) and crossbar arrays for the next generation of computer architecture.



Wei D. Lu is a Professor in the Electrical Engineering and Computer Science department of the University of Michigan. He received a B.S. in physics from Tsinghua University in 1996, and a Ph.D. in physics from Rice University in 2003. His research interests include resistive random access memory (RRAM)/memristor devices and neuromorphic systems, aggressively scaled transistor devices, and low-dimensional systems.

Solid-state resistive switching devices driven by nanoscale ionic processes are reviewed, with focus on the rich ionic dynamics that enable natural implementation of diverse biological synaptic and neuron functions. Efforts to control ion redistribution at the atomic scale have led to improved device performance, and enabled applications based on reconfigurable nanostructures and materials through controlled ionic processes in solid-state devices.

Neuromorphic Computing



Authc